46th AIAA Aerospace Sciences Meeting and Exhibit
7 - 10 January 2008, Reno, Nevada

AIAA 2008-836

Stall Behaviour of the EUROLIFT High Lift Configurations

R. Rudnik*
DLR, German Aerospace Center, 38108 Braunschweig, Germany

Based on a previous analysis of the high lift performance of a commercial aircraft-type high lift configuration in terms of lift curves and drag polars and their Reynolds-number dependency a detailed study of the corresponding stall behavior is carried out. It is part of extensive experimental research activities on the aerodynamics of high lift configurations within the European projects EUROLIFT (I) and II. The investigations are conducted using the KH3Y wind tunnel model (DLR F11), which is representative for a wide-body twin-jet commercial aircraft. The model is designed for a step by step complexity increase up to a complete high lift configuration including pylon, nacelle, and nacelle strake. The wind tunnel data have been gathered in the European Transonic Windtunnel ETW in two different test campaigns. The Reynolds-number range extends from Re ~ 2.3 x 10^6 up to Re ~ 25 x 10^6. To analyze the stall behavior spanwise pressure distributions at maximum lift and at lift breakdown are compared for two limiting Reynolds-numbers for each of the four complexity stages of the KH3Y configuration. The investigation reveals that for the clean high lift wing without nacelle stall is triggered at the outboard sections of the fixed wing. When the nacelles are added the lift breakdown starts on the fixed wing inboards of the nacelle. Adding a nacelle strake alleviates the lift breakdown inboards of the nacelle, while lift breakdown still occurs around the spanwise position of the nacelle on the fixed wing. For none of the four configurations a significant change of the stall type is observed for the considered Reynolds-number conditions. Yet, the investigation of the most complex configuration with strake reveals, that the effectiveness of the strake and its interaction with the flow on the fixed wing is subject to Reynolds-number influences.

Nomenclature

A	=	reference area
c_p	=	pressure coefficient
C_L	=	total lift coefficient
C_D	=	total drag coefficient
c_{ref}	=	mean aerodynamic chord
DV	=	pressure section
l	=	length
lcts.	=	lift count = 0.01
M	=	Mach number
p	=	static pressure
q	=	dynamic pressure
Re	=	Reynolds number based on c_{ref}
STR	=	Short Term Repeatability
s	=	model half span
T	=	temperature
VHBR	=	Very High Bypass Ratio
WP	=	geometrical window point for flap rigging

subscripts

f	=	flap
max	=	maximum of a specific quantity
s	=	slat
t	=	total quantity
∞	=	free stream value

greek symbols

α	=	angle of attack
α_1	=	angle of attack in the linear lift regime
α_2	=	angle of attack at maximum lift
α_3	=	angle of attack at lift breakdown
δ_f	=	flap deflection angle
δ_s	=	slat deflection angle
η	=	non-dimensional span; η = y/s
Λ	=	aspect ratio
λ	=	taper ratio

* Head Transport Aircraft, Institute of Aerodynamics and Flow Technology, Lilienthalplatz 7, 38112 Braunschweig.

I. Introduction

THE present study is complementary to an investigation of the aerodynamic properties and their Reynolds-number scaling effects of a commercial aircraft-type configuration with deployed high lift devices described in Ref. 1. The investigations are based on results obtained throughout two consecutive European projects on high lift aerodynamics, EUROLIFT (I) and EUROLIFT II. While EUROLIFT (I) has been launched as part of the 5th European Framework Programme in 1999 under the co-ordination of Airbus-Deutschland, EUROLIFT II has been part of the 6th European Framework Programme and has been coordinated by DLR. EUROLIFT II has been finalized in spring 2007. The main objective of both collaborative projects is to further improve the understanding of high lift aerodynamics on realistic commercial-type aircraft configurations featuring a fuselage, a high lift wing with different leading and trailing edge devices, and high bypass ratio nacelles mounted under the wing. In addition, the influence of a strake is investigated as a vortex generating device placed on the outer nacelle contour to improve the maximum lift performance. In both projects extensive experimental as well as numerical investigations are carried out. The general approach is to utilize both methodological areas complementary and in close collaboration. Consequently CFD code validation represents a major focus of the projects. In addition to the analysis of complex 3D high lift configurations major areas of research cover the fields of improvements of numerical and experimental tools[2,3], transition prediction[4], and numerical optimization of high lift devices[5]. An overview about both projects and related literature can be found in Ref. 6 to Ref. 8. Regarding high lift aerodynamics of transport aircraft in general, a large number of studies has been published focusing either on high lift design considerations of specific aircraft including Reynolds-number scale effects, e.g. Ref. 9 and Ref. 10 or on general high lift design aspects as in Ref. 11. In addition, several investigations have been carried out for the purpose of validation and improvement of theoretical methods for high lift flow problems. A very comprehensive study including wind tunnel models of different scales and flight testing is conducted within the framework of GARTEUR is described in Ref. 12. Other validation activities are found in Ref. 13 and Ref. 14.

Despite the variety of investigations in the field of high lift aerodynamics the request to generate a database to address and analyze the influence of configuration features relevant for a typical commercial aircraft high lift configuration over a large range of Reynolds-numbers motivated the launch of the EUROLIFT projects. The baseline wing/fuselage geometry used for this purpose in both projects is denoted as KH3Y, the corresponding wind-tunnel model, manufactured by DLR, is designated DLR-F11. The model is used in four different complexity stages starting with a fuselage and a simplified three-element high lift wing up to a configuration with pylon, nacelles and a nacelle strake. The intention of the subsequent complexity increase is to identify and separate the effects of the single components on the high lift performance. The model is consistently wind tunnel tested using the different complexity stages in two facilities. The first one is the low speed wind tunnel of Airbus-Deutschland, B-LSWT. These low Reynolds-number tests under atmospheric conditions have enabled the use of various advanced flowfield measurement techniques like 3-component PIV to provide detailed insight into the dominant flow phenomena[15]. The second involved facility is the European Transonic Windtunnel ETW which is used to address Reynolds-number scaling effects by covering a broad range from low Reynolds-numbers up to flight conditions.

In Ref. 1 a survey of the general scale effects is given which have been observed on the four complexity stages of the KH3Y configuration with the high lift devices in landing setting. The data have been gathered throughout a series of test campaigns in the ETW carried out in both EUROLIFT projects. The focus of the analysis has been laid on the high lift performance in the linear lift regime and the attainable maximum lift for different Reynolds-numbers. For this purpose basically lift curves and drag polars have been analyzed. When comparing the results for low atmospheric to highly cryogenic conditions, a favorable Reynolds-number influence on the overall aerodynamics has been observed. Nevertheless, also distinct adverse scaling effects have been found with respect to maximum lift in the Reynolds-number range between $Re \sim 5 \times 10^6$ and $Re \sim 10 \times 10^6$, when nacelle and pylon have been added to the configuration. Moreover, the strake efficiency observed in the low Reynolds-number tests has been compromised at the highest Reynolds numbers. The intention of the present study is to investigate the maximum lift trends and the stall behavior in more detail.

In general maximum lift on high aspect ratio wings and configurations is directly related to the occurrence of flow separation. Limited areas of flow separation can be found on components of the wing before maximum lift is reached. This is observed oftentimes on highly deployed trailing edge flaps in a landing setting at low and moderate angles of attack. As long as the lift generation on the other components is strong enough to over-compensate the loss of lift in the separation zones, the overall lift is still in creasing with angle of attack. For highly deployed flaps the flow usually attaches at higher angles of attack around maximum lift. Typically extended flow separation on the fixed wing then causes the overall lift to decrease after maximum lift has been reached. This phenomenon is called lift breakdown or stall. To the author's knowledge no clear differentiation between both expressions exists. Stall is usually regarded as a flight condition of an aircraft, for which excessively high angles of attack or insufficient airspeed cause a loss of lift and an unstable flight condition. Together with load and safety factors the corresponding stall speed is used within the certification procedure to determine take-off and landing speeds. Lift breakdown might refer more to the lift reduction process of the wing after maximum lift is reached. Essentially both expressions refer to the same aerodynamic effect and both are used in a compatible manner throughout this text. A variety of stall phenomena and mechanisms exists. The present study focuses on the lift breakdown of a high aspect ratio wing with deployed high lift devices. As described in Ref. 16 basically four different stall types are distinguished for a simple single element airfoil: thin airfoil stall, leading edge stall, combined leading and trailing edge stall, and trailing edge stall. The occurrence of a specific stall type is related to the airfoil geometry and the onflow Reynolds-number. The knowledge and understanding of the dependency of aerodynamic properties in general and the stall type in particular from the Reynolds-number is essential to extrapolate aerodynamic results from sub-scale wind-tunnel tests to flight conditions. As described in Ref. 17 four sources of direct scale effects are relevant for multi-element high lift wings. These are conventional scale effects associated with the reduction of the boundary layer thickness with increasing Reynolds-number and the ability of the boundary layer to withstand higher pressure gradients without separating, bubble dominated scale effects related to changes in the characteristics of a laminar separation bubbles, slot flow dominated scale effects, which typically characterize the viscous interaction between the wake of an upstream element with the boundary layer of a downstream element, and finally transition dominated scale effects.

While the stall type of a single element airfoil can be usually identified by the slope of the lift curve, the situation on complete 3D high lift transport aircraft configurations is much more complicated. The wing taper leads to spanwise varying local Reynolds-numbers and consequently the scale effects on the maximum attainable lift change with span. The fact that often elements of the wing still produce lift with increasing angle of attack whereas on others the lift is already breaking down requires an in detail study to characterize the type of lift breakdown. The knowledge of the effects and location of the lift breakdown is crucial to improve the high lift performance by design changes. In addition to the shape and the relative setting of the wing and its high lift devices the engine airframe interference of underwing mounted engines plays a vital role in determining and improving the high lift performance. Critical areas are the wing root, the leading edge area at the nacelle position, and the outer wing area, all characterized by cut-outs or cut-backs of high lift devices. The most complex configuration of the present study is equipped with a nacelle mounted on a pylon and focuses on the first two of the features listed before. As mentioned the general high lift performance in terms of lift and drag coefficients has been investigated in Ref. 1. Fig. 1 is taken from Ref. 1 and summarizes the results in terms of maximum lift of the four complexity changes vs. Reynolds-number.

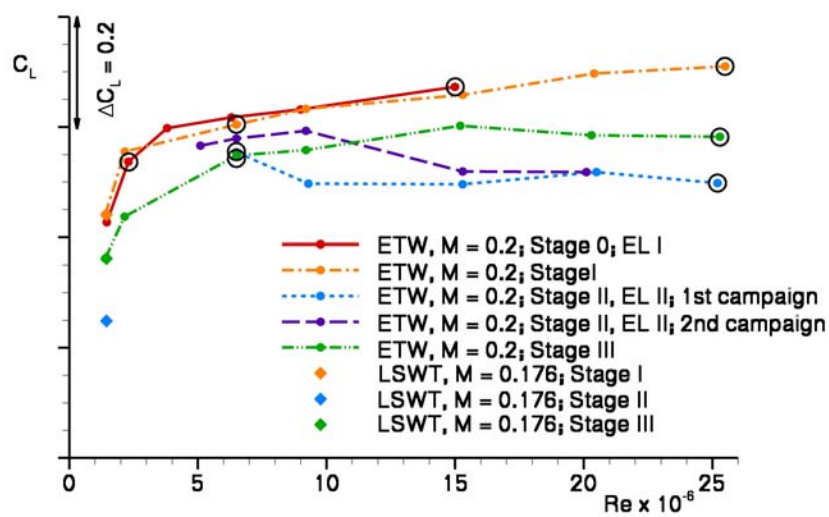

Fig. 1 Maximum lift coefficients for different Reynolds-number and KH3Y complexity stages

The present contribution is intended to delve into the aerodynamic properties of the KH3Y configuration and extend the analysis of the experimental results with a focus on the stall behavior of the different complexity stages.

Due to the amount of data for the different Reynolds-numbers various ways are conceivable to accomplish this task. The approach taken in this study is driven by the following considerations:

- The baseline assessment of the stall characteristics is done by comparing a low and a high Reynolds-number condition for an identical configuration
- In order to compare the different complexity stages of the configuration similar Reynolds-numbers should be selected for the evaluation

As far as the upper range is concerned the highest available Reynolds-number Re ~ 25 x 10^6 is selected, although no data for the simplest configuration are available at this Reynolds-number. For the low Reynolds number Re = 6.5 x 10^6 is selected. The reason is that Re = 6.5 x 10^6 represents the lowest Reynolds-number for which experimental results of all configurations are available for the Mach number of $M_\infty = 0.2$. Moreover, this Reynolds-number is in the range in which adverse scale effects have been found, enforcing the interest in analyzing this condition. It has to be noted, that Re = 6.5 x 10^6 is already beyond the Reynolds-number, that can be realized in purely atmospheric windtunnel facilities on complex configurations. On the other side this condition is fairly representative for non-cryogenic facilities that operate with increased total pressure. Thus, the term 'low Reynolds-number' condition has to be regarded in this sense. The test of configuration Stage 0 has been carried out in a EUROLIFT (I) campaign in the ETW. As a consequence the Reynolds-number range is not consistent with the other configurations. In order to select conditions for this configuration, which are fairly comparable to the others the two limiting Reynolds-numbers Re = 2.3 x 10^6 and Re = 15 x 10^6 have been chosen. All selected Reynolds-number conditions for the present study are indicated by black circles in Fig. 1

The main experimental evidence to assess the maximum lift and stall behavior will be the lift curves and the spanwise pressure distributions. As the aerodynamic effects are exclusively related to the lift generation drag issues are not discussed in the present context.

II. KH3Y Configuration and Test Set-Up

The baseline geometry for the present studies is a commercial wide-body twin-jet high lift configuration. The wind tunnel model consists in its most complex configuration of a wing/fuselage configuration with a high bypass ratio through-flow-nacelle with core body. The high lift system has a leading edge slat and a trailing edge Fowler flap. For the present studies only the landing setting is considered, as the major interest is in the maximum lift performance. The main dimensions of the model are listed in Table 1:

Table 1: Main dimensions of KH3Y high lift model

half span, s	[m]	1.4
wing reference area, A/2	[m^2]	0.41913
reference chord, c_{ref}	[m]	0.34709
aspect ratio, Λ	[-]	9.353
taper ratio, λ	[-]	0.3
¼ chord sweep, φ_{25}	[^{o}]	30
fuselage length, l_{Fu}	[m]	3.077
slat deflection angle, δ_s	[^{o}]	26.5
flap deflection angle, δ_f	[^{o}]	32.0

The through-flow-nacelle is mounted at 34% half span. It is representative of a modern VHBR-engine with a bypass ratio of about 10 with external mixing. The nacelle diameter is 0.155 m, the overall length amounts to 0.33 m. It is closely coupled to the wing. The inlet lip design is adjusted to high lift conditions. A nacelle strake is mounted inboard on the nacelle. A slat cut-out is introduced at the fuselage intersection. At the inner slat-end an onglet serves as a fairing between wing leading edge and fuselage. The inner slat side edge is equipped with a slat-horn. For the wing/fuselage/nacelle configuration the slat has a realistic cut-out at the pylon/slat junction. The reference setting for the landing configuration is denoted as WP 9. For all experiments of the EUROLIFT projects the model is tested as a half model mounted on a Peniche. The high lift wing is equipped with 487 pressure taps in

10 pressure sections (DV). Pressure section 3 is not available for the high lift model. A planform view of the wing including the location of the pressure sections is shown in Fig. 2.

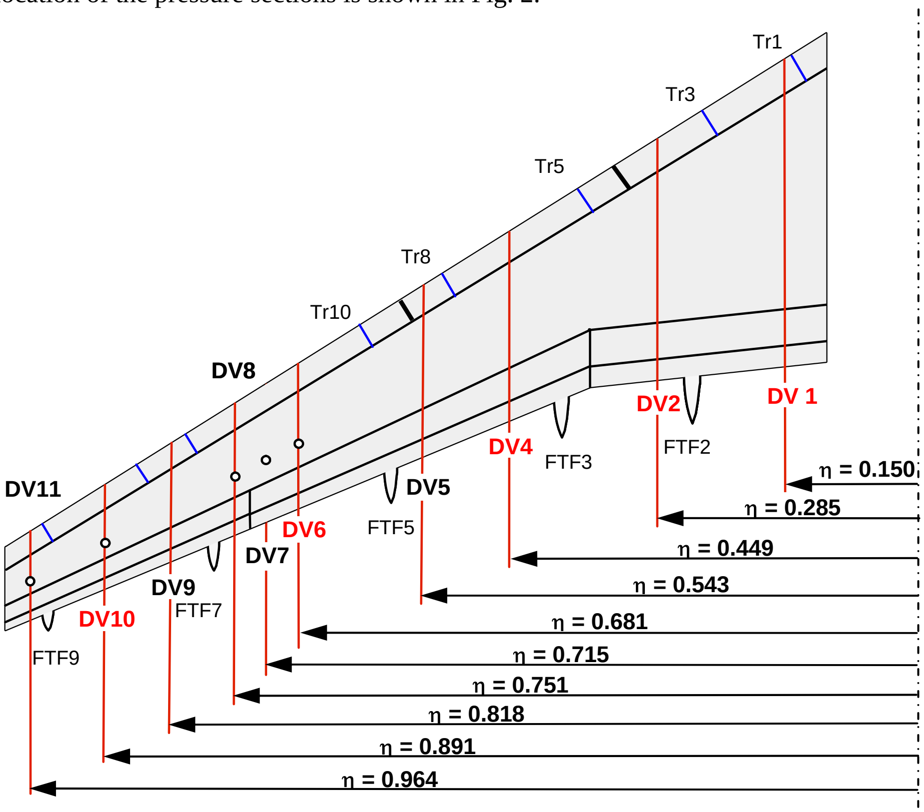

Fig. 2   KH3Y high lift configuration Stage 0 with model instrumentation

The through-flow-nacelle has an internal core-body and an internal pylon. It is equipped with a pressure plotting instrumentation at two longitudinal sections of the outer nacelle at radial positions of 30° (outboard) and 330° (inboard) using 30 pressure taps. The KH3Y windtunnel model with engine and pylon is shown in Fig. 3.

Fig. 3   KH3Y high lift configuration with nacelle and pylon

The analysis of the scaling effects will focus on four different levels of complexity, denoted as Stage 0 to Stage III. Stage 0 is the baseline simplified configuration with full span slat and flap. For Stage I a realistic slat end with onglet and slat horn at the fuselage is introduced. For Stage II the pylon/nacelle components are added. Stage III is characterized by the addition of the inboard nacelle strake. The different complexity levels are depicted in Fig. 4.

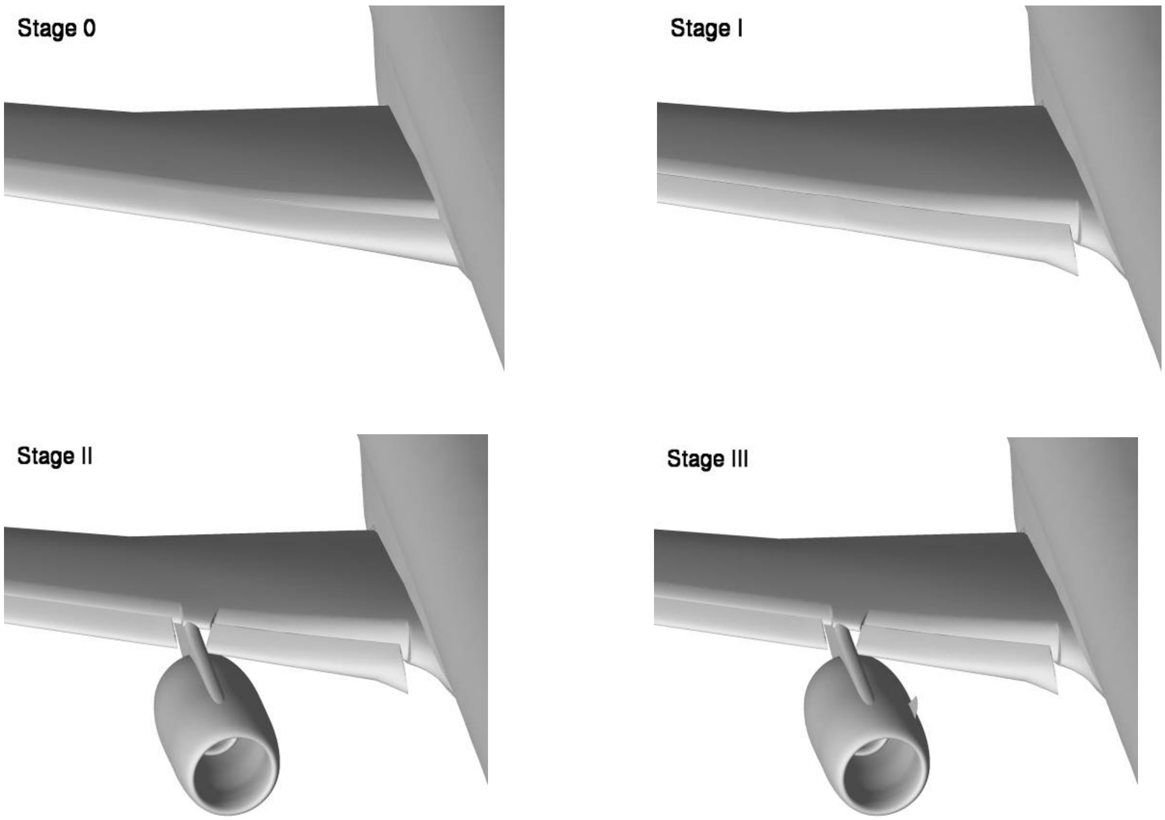

Fig. 4 Complexity levels of the KH3Y high lift configuration

All experimental data discussed in the following have been gathered in the European Transonic Windtunnel (ETW) facility in Cologne, Germany. The ETW has a closed aerodynamic circuit with a Mach number range from M = 0.15 to 1.3. The test section is 2.00 m high, 2.40 m wide, and 8.73 m long and is used with closed slots in the tunnel walls for the present tests. In addition to pressure and force measurements, minitufts are applied to the wing upper surface in the area of the engine mounting to provide additional flow visualization of the wing stalling process. To determine wing and high lift system deformation an existing SPT as well as an ESPT (Enhanced Stereo Pattern Tracking system) system has been applied.

The test data under consideration have been collected during two of three test campaigns in the ETW throughout the runtime of both EUROLIFT projects. The first ETW test campaign took place in summer 2002 in the framework of EUROLIFT (I). In this campaign the data for configuration Stage 0 with a Reynolds-number range from Re = 1.45×10^6 up to 15×10^6 have been taken. The second campaign in spring 2005 was part of EUROLIFT II. In this campaign data for configurations Stage I, II, and III have been recorded with a Reynolds-number range from Re = 6.5×10^6 up to 25×10^6. These ETW tests are accompanied by tests in the low speed tunnel of Airbus-Deutschland in Bremen, B-LSWT, in early 2005 for Re = 1.4×10^6. The main focus of this atmospheric test has been to gather detailed flow field information on the vortex dominated interaction of the high lift wing with engine, pylon, and strake using surface and field measuring techniques as oil flow, hot films, and 3-component PIV. A description of the results of the B-LSWT test is given in Ref. 15. More details on the wind tunnel model and the test facility are found in Ref.1 and Ref. 3.

III. Experimental Results

The results discussed in the following have been obtained in the ETW for an onflow Mach number of $M_\infty = 0.2$ with the high lift devices in the landing setting according to WP9. The total temperature and dynamic pressure have been varied to generate the different Reynolds-number conditions. The focus of the present investigation is laid on the stall behavior of the four considered configurations and thus the lift generation. Primarily pressure distributions along the wing span will be analyzed for selected angles of attack. In contrast to Ref. 1 only results of the lowest and highest available Reynolds-number are evaluated. To select the relevant angles of attack and the spanwise pressure stations the following approach is applied. Based on the lift curves for the respective low and high Reynolds-number conditions three relevant flow regimes are considered. The first flow condition is assigned to the angle of attack at which maximum lift is attained, designated as α_2. To analyze the stall behavior a second angle of attack is required, at which a clear lift breakdown has occurred, designated as α_3. In order to assess the magnitude of the lift breakdown, these two flow conditions are accompanied by a third angle of attack in the linear lift range α_1. This angle of attack corresponds to total lift coefficients somewhat below $C_L = 2$ and is supposed to be fairly representative for flight attitudes. Usually α_2 and α_3 vary with Reynolds-number and configuration.

The analysis of the stall behavior is then accomplished by comparing five out of ten measured pressure distributions to assess the lift breakdown on the high lift elements along the span. The pressure distributions are DV 1, DV 2, DV 4, DV 6, and DV 10. From those a critical section with respect to the lift breakdown is selected to analyze in more detail the development of the pressure distribution for the three angles of attack. This is done separately for low and high Reynolds-numbers. Finally, the direct comparison of the pressure distributions for the low and high Reynolds-number conditions at maximum lift is carried out in two relevant pressure sections. The selection of the most relevant pressure sections is depending on the configuration.

The pressure distributions for the single elements are normalized in the chordwise direction with the local chord of the respective element. Note that the scale on the ordinate is adapted to the valid pressure range of the respective element in the 2D sketches. Yet, all pressure plots use the same origin for the single elements as well as for the lift distributions, so that the graphs can be compared directly.

A. Configuration KH3Y Complexity Level Stage 0

The data of the Stage 0 configuration are gathered in the ETW during the EUROLIFT (I) project. The configuration is the most simplified one of the KH3Y model. The high lift system consists of a continuous full span slat and flap. Both intersect with the fuselage without a spanwise gap, see Fig. 4. In order to achieve a Reynolds-number variation from $Re = 2.3 \times 10^6$ up to 15×10^6 for the given Mach number of $M_\infty = 0.2$, the dynamic pressure is varied from q = 4.2 up to 6.9 kPa. The total temperature varies from $T_t = 300$ K down to 115 K.

Due to the lack of the engine/pylon components it is to be expected that the maximum lift and stall behaviour of this configuration is dictated by the sectionwise high lift properties. The lift curves for the low and high Reynolds-number cases are depicted in Fig. 5. Both curves show a rounded comparatively wide maximum lift area. Following Table 2 the angle of attack of maximum lift is not affected by the Reynolds-number for the two considered extreme cases. The studies in Ref. 1 show that this doesn't hold for the intermediate Reynolds-numbers.

Table 2: Characteristic angles of attack for KH3Y configuration Stage 0

Angle of attack		$Re = 2.3 \times 10^6$	$Re = 15.0 \times 10^6$
α_1	[°]	7.04	7.04
α_2	[°]	20.02	20.02
α_3	[°]	23.09	23.10

In general, a clear favorable scale effect with Reynolds-number is visible. An increase in maximum lift of nearly 14 lcts. is found for the high Reynolds-number. For this case also a distinct lift breakdown is observed beyond maximum lift with a lift decrease of about 42 lcts. from α_2 to α_3. For the low Reynolds-number the lift at α_3 is only slightly decreasing by about 5 lcts. compared to the maximum lift value.

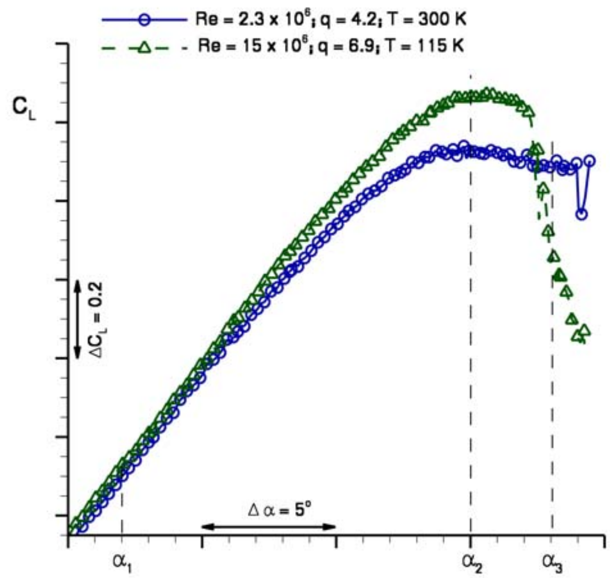

Fig. 5 Lift curve for low and high Re-number for the KH3Y complexity Stage 0

The corresponding pressure distributions along the wing span on the slat, the fixed wing, and the flap are shown in Fig. 6 at the angle of maximum lift α_2 and an angle of lift breakdown α_3 for the low Reynolds-number condition. While the suction peaks of the slat pressure distributions are still clearly increasing from α_2 to α_3, lift breakdown is caused by the main wing and the flap. Stall occurs due to trailing edge separation on both elements. It is visible starting at the midboard station DV 4 with increasing tendency towards the wing tip. It should be noted, that this statement is not referring to the beginning of separation and stall on single elements, which typically occurs already at angles of attack smaller than α_2, but directly applies to the comparison of the pressure distributions at α_2 and $\alpha_{3.}$ For the present case section DV10 is a critical wing section worth to be analyzed in more detail. The pressure distribution at section DV 10 is displayed in Fig. 7 for the two angles of attack discussed before, as well as for as the angle of attack representative for the linear lift regime. Looking at the development of the pressure distributions with increasing angle of attack, it can be concluded that there is attached flow on the slat up to $\alpha_{3.}$ Moreover, the slat pressure distribution shows the strongest increase in the suction level and thus in lift from the linear range to the maximum lift condition. The evaluation of the inboard stations in Fig. 6 reveals that the suction level on the slat upper surface is even considerably increasing from α_2 to α_3. This effect might compensate the clear lift breakdown on the other elements and thus alleviate the overall lift breakdown resulting in the smooth lift curve in Fig. 5. Nevertheless, it has to be taken into account that the slat contributes only by about 20% to the total lift, due to its smaller chord length and its deflection angle. The outboard pressure distribution on the fixed wing reveals, that the highest suction peak and consequently the highest lift generation takes place for the maximum lift condition. After maximum lift a trailing edge separation is building up. In contrast to this the flap upper surface pressure level is monotonously increasing from α_1 to the highest evaluated angle of attack α_3, diminishing the lift generation. Already at maximum lift condition more than 50% chord of the flap upper surface appears to have separated flow. As a consequence the lift breakdown on the flap beyond maximum lift is weaker than on the fixed wing. This is endorsed by the fact, that the pressure level in the separated trailing edge area is lower for α_3 than for α_2, an effect which is probably caused by the velocity field induced by the fixed wing trailing edge and its wake.

Moving on to the high Reynolds-number case some differences in the stall behavior are found, see Fig. 8. The most pronounced difference compared to the low Reynolds-number case is observed for the slat. Especially at the outboards stations DV 6 and DV10 a strong lift breakdown and large areas of trailing edge separation are observed for α_3, while the suction peaks are still increasing at the inboard stations. For the main wing the tendency of the low Reynolds number case is maintained, featuring an increasing amount of trailing edge separation towards the outboard pressure sections. Compared to the low Reynolds-number case the differences between the pressure levels of α_2 and those of α_3 are clearly larger.

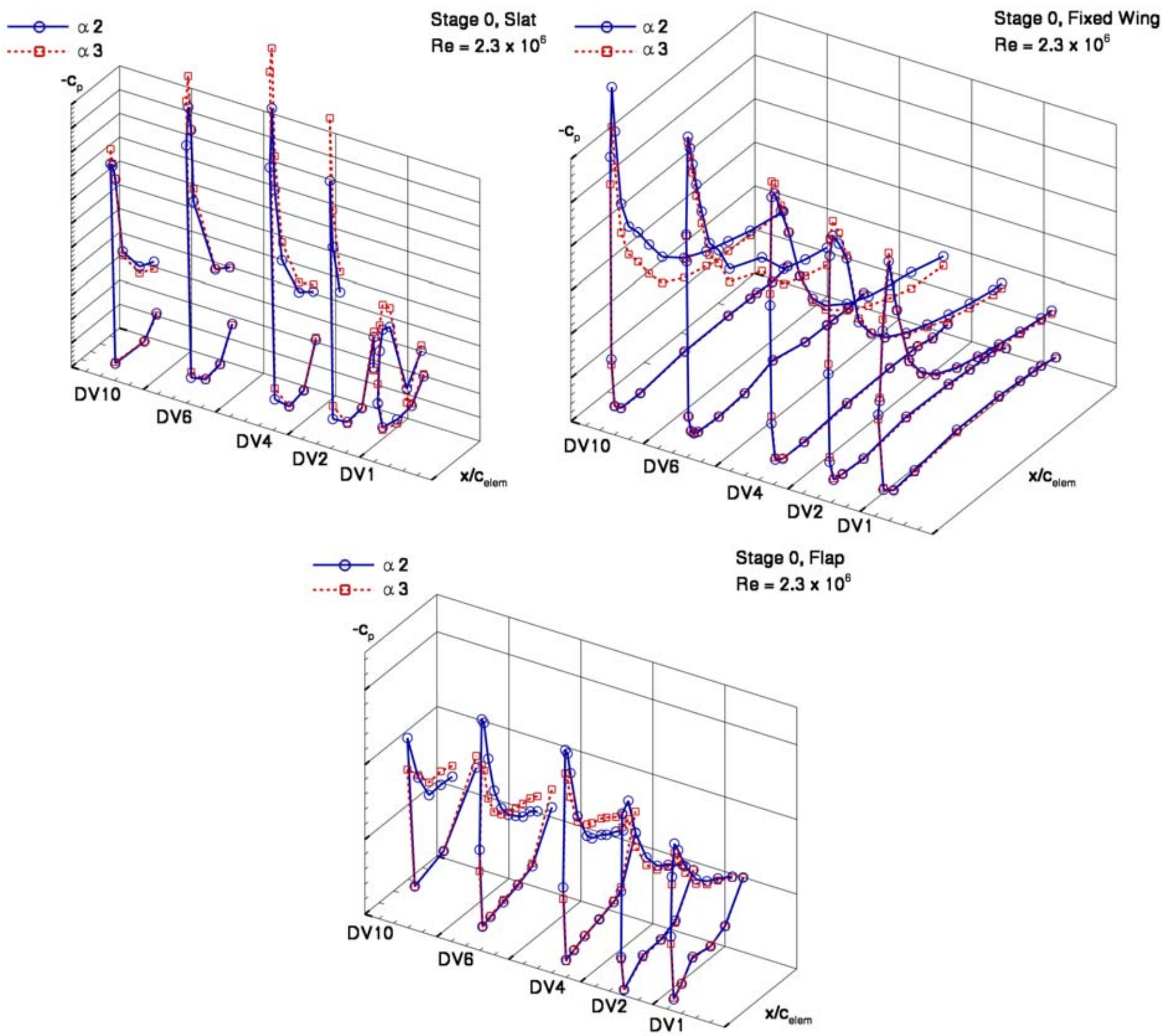

Fig. 6 Pressure distributions at and beyond maximum lift at low Re-number conditions

The lift breakdown on the flap is in general quite similar to that of the low Reynolds number case. The pressure distribution at section DV 10 for the three distinct angles of attack at high Reynolds-number conditions, Fig. 9, confirms these observations. For the high Reynolds-number conditions the largest lift on the slat is now generated at α_2, followed by a clear lift breakdown at α_3. The development on the fixed wing is in general similar to the low Reynolds-number case, but the increase in pressure level for α_3 is more pronounced. On the flap the decrease in lift is again starting already at α_1. Yet, the amount of trailing edge separation especially at α_2 appears to be reduced compared to the low Reynolds-number case. In summary the more abrupt lift breakdown for the high Reynolds-number case of configuration Stage 0 is caused by two effects. On the one hand side a strong lift breakdown is observed on the slat. Especially at the spanwise position of DV 6 this seems to be due to a strong trailing edge separation on the slat. Given the Reynolds number a bursting of a laminar separation bubble seems unlikely as fully turbulent flow can be assumed. The second effect is the stronger lift loss due to trailing edge separation on the outboard portion of the fixed wing.

Finally, a direct comparison of an inboard and an outboard pressure section at the respective angle of attack for maximum lift is given in Fig. 10 and Fig. 11. At the inboard station, DV 2, only minor differences are found with a slightly higher suction peak on the slat and the flap for the high Reynolds-number case. The differences are much more pronounced for the outboard section, DV 10, in Fig. 11. The suction peaks are considerably higher on all three elements, featuring a suction pressure difference between low and high Reynolds number case of $\Delta c_p \sim 1$ for the slat

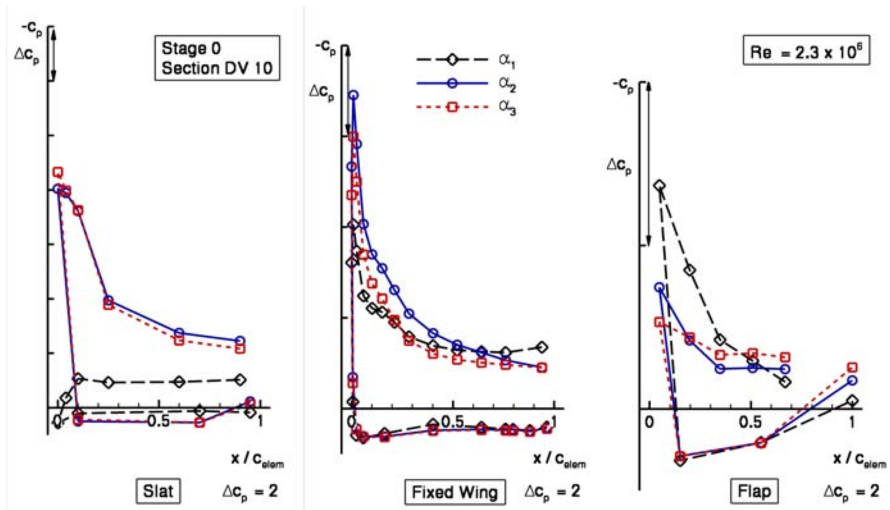

Fig. 7 Outboard pressure distribution at different angles of attack for low Re-number conditions

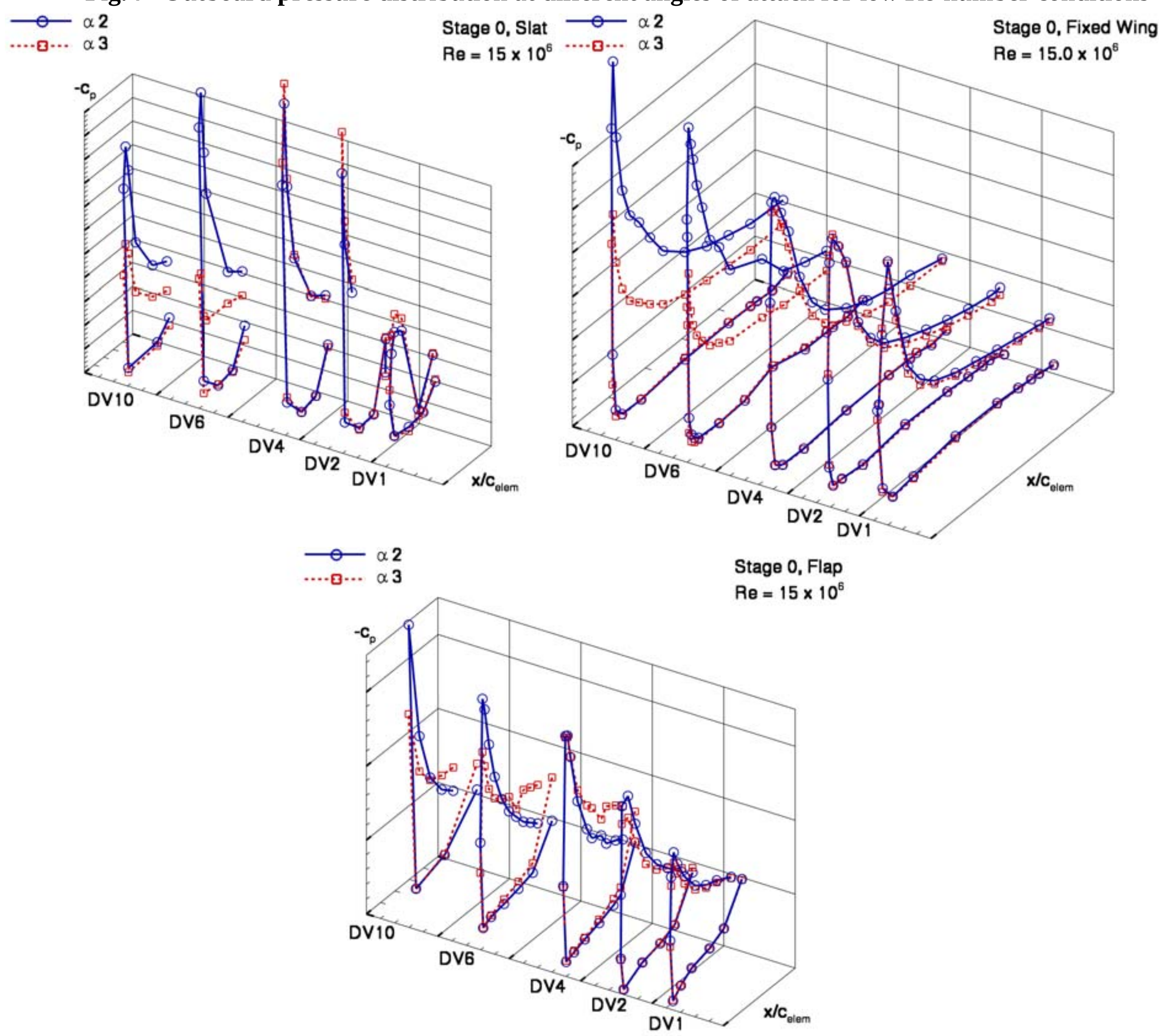

Fig. 8 Pressure distributions at and beyond maximum lift at high Re-number conditions

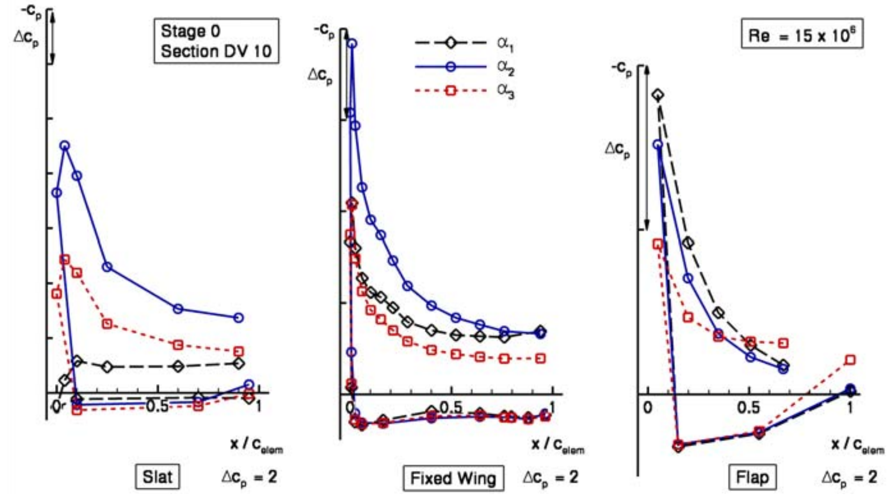

Fig. 9 Outboard pressure distribution at different angles of attack for high Re-number conditions

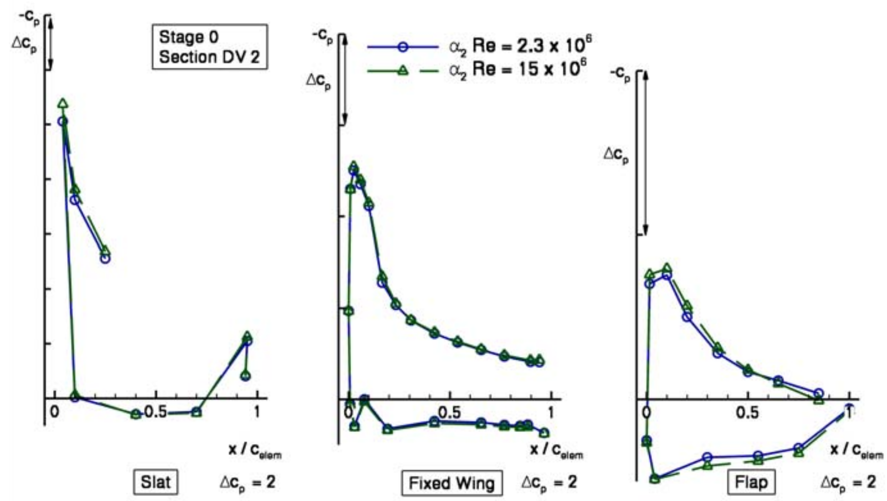

Fig. 10 Inboard pressure distribution at maximum lift for low and high Re-number conditions

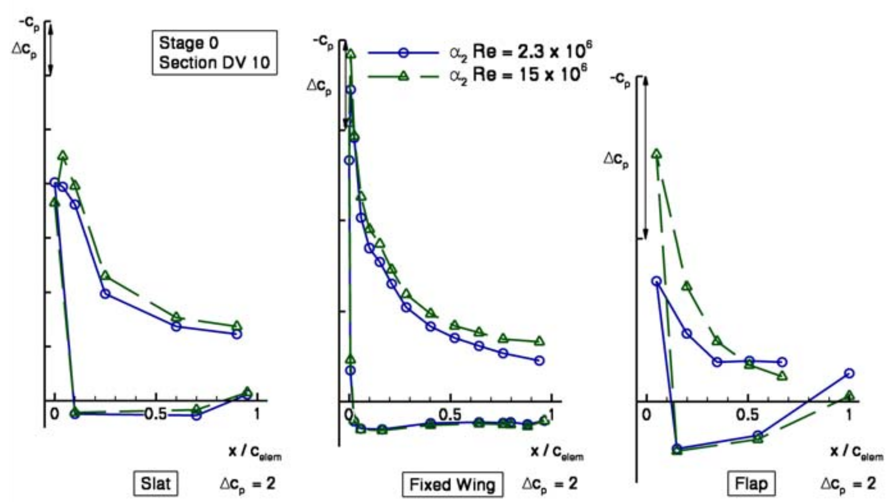

Fig. 11 Outboard pressure distribution at maximum lift for low and high Re-number conditions

and the fixed wing, while a value of $\Delta c_p \sim 1.5$ is observed for the flap. Consistent with the size of the suction peaks the pressure level over the upper surface of slat and fixed wing is lower for the higher Reynolds-number case. For the flap, the trailing edge separation has vanished for Re = 15 x 10^6. Typically, this is an indication that the flap gap is optimized for high Re-number conditions. Yet, it is worth mentioning that in the present case this strong Reynolds number effect in maximum lift and lift breakdown is more or less confined to the outboard half of the wing.

B. Configuration KH3Y Complexity Level Stage I

The difference between the KH3Y configurations Stage 0 and Stage I lies in the wing/fuselage intersection. For configuration Stage I a spanwise cut-out of the slat is introduced at the fuselage. In addition to the cut-out itself also a fuselage fairing designated as onglet as well as a slat horn are added, see Fig. 4. The two limiting Reynolds-numbers of the EUROLIFT II campaign in the ETW have been selected for comparison and assessment of the stall behavior. The low Reynolds-number case at Re = 6.5 x 10^6 is characterized by a dynamic pressure of q = 4.2 kPa and a total temperature of T_t = 138 K. The high Reynolds-number case with Re = 25.5 x 10^6, is defined by a dynamic pressure of 12.6 kPa and a total temperature of T_t = 138 K. The corresponding lift curves are depicted in Fig. 12.

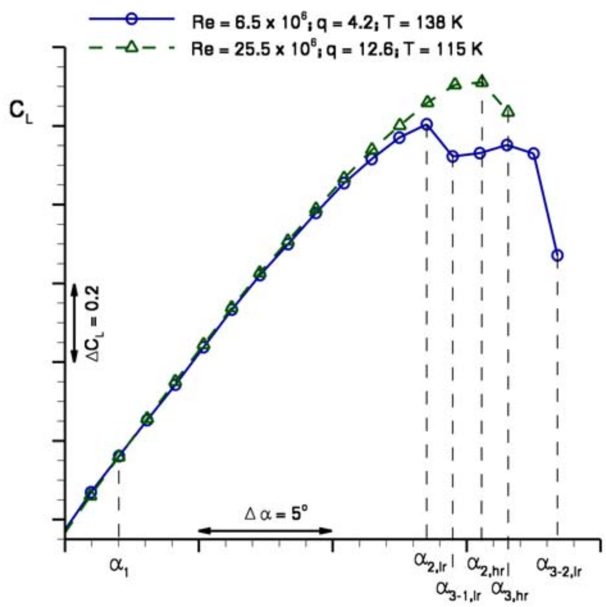

Fig. 12 Lift curve for low and high Reynolds-number for the KH3Y complexity Stage I

Again a favorable scale effect is found with a lift increase of $\Delta(C_{L,max}) \sim 0.11$. A noted in Table 3 in this case there is a considerable difference in characteristic angles of attack for low and high Reynolds numbers. The angle of attack for maximum lift, α_2, is about 2^o larger for the high Reynolds-number case.

Table 3: Characteristic angles of attack for KH3Y configuration Stage 0

Angle of attack		Re = 6.5 x 10^6	Re = 25.5 x 10^6
α_1	[^{o}]	7.02	7.01
α_2	[^{o}]	18.51	20.58
α_{3-1}	[^{o}]	19.48	-
α_{3-2} / α_3	[^{o}]	23.39	21.55

Although a thorough comparison between configuration Stage 0 and Stage I is not possible, because the Reynolds-numbers themselves as well as their differences are different for both stages, the smooth slope around maximum lift for high Reynolds-number cases of Stage 0 and Stage I seems similar indicating that again a trailing edge stall may prevail. In contrast to this the slope of the low Reynolds-number cases are clearly different. For configuration Stage I the total lift is decreasing by a $\Delta(C_L)$ of about 0.08 after maximum lift is reached and remains at about this level until finally a clear lift breakdown with a further drop in C_L of about 0.25 occurs. As this behavior is observed somewhat frequently on 3D high lift configurations is seems worth while to analyze it in more detail. Therefore, two post-maximum lift angles $\alpha_{3\text{-}1}$ and $\alpha_{3\text{-}2}$ are introduced for the low Reynolds-number condition to investigate the pressure distributions at the first slight lift breakdown and at the final clear stall. The corresponding selected pressure sections along the span at α_2 and at $\alpha_{3\text{-}1}$ are displayed in Fig. 13.

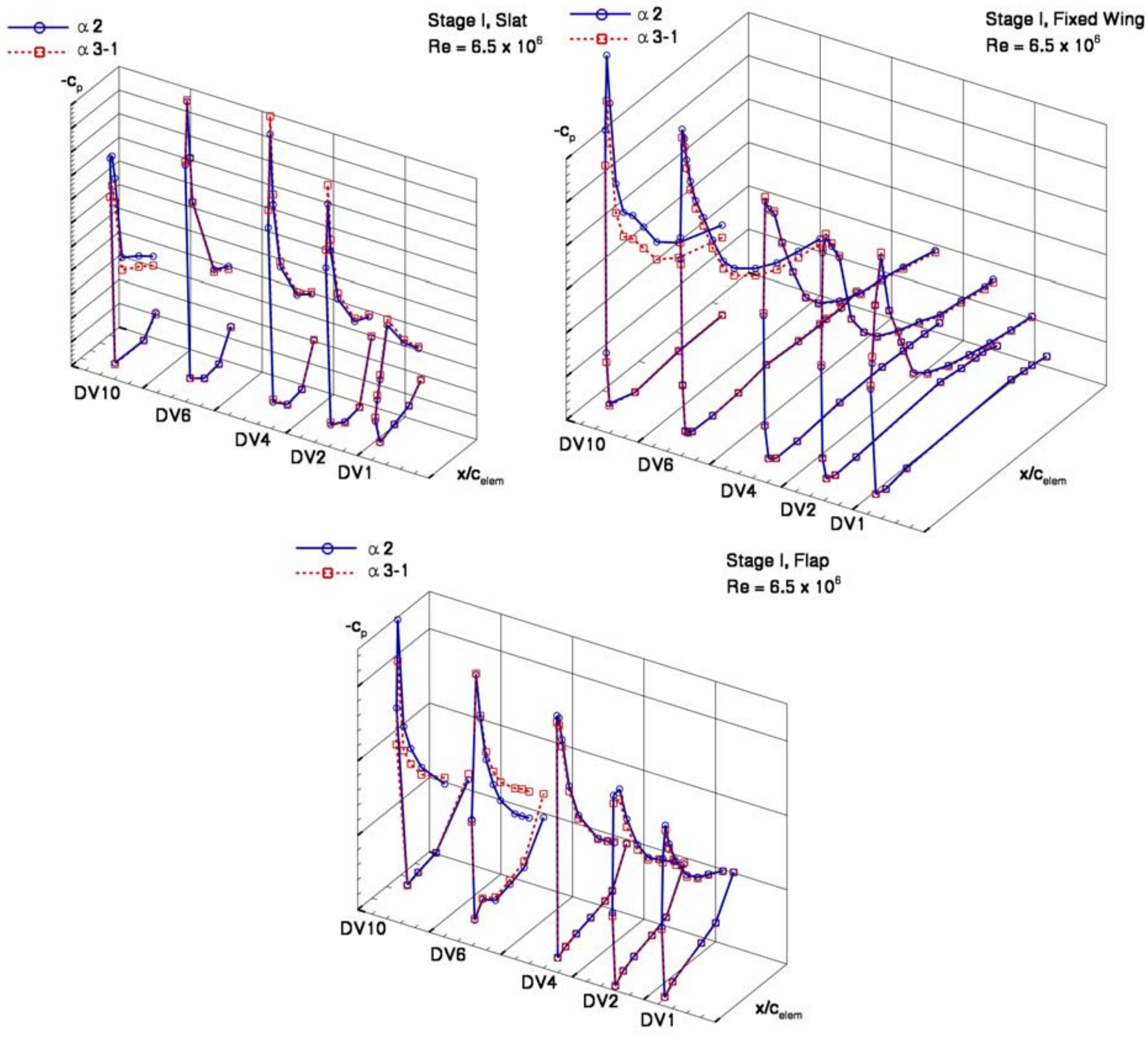

Fig. 13 Pressure distributions at and slightly beyond maximum lift for low Re-number conditions

The slight lift breakdown from α_2 to $\alpha_{3\text{-}1}$ has its origin in a lift loss on the outboard part of the wing, visible at sections DV 6 and DV 10. All three elements are part of this effect with the fixed wing dominating the loss in lift. The strongest overall difference is found on the flap at DV 6, where the trailing edge pressure level is decreasing. As the corresponding suction peak remains unaffected, the resulting lift produced by the flap is slightly higher than that at maximum lift and thus potentially compensates somewhat the lift loss at DV 10. In general no severe differences are observed between the pressure distributions at the two angles of attack. Following the pressure distributions attached flow is clearly prevailing. While the difference in angle of attack in Fig. 13 amounts to only 1^o, a difference of about 4^o until a clear lift breakdown is displayed in Fig. 14, comparing the pressure distributions at $\alpha_{3\text{-}1}$ and $\alpha_{3\text{-}2}$.

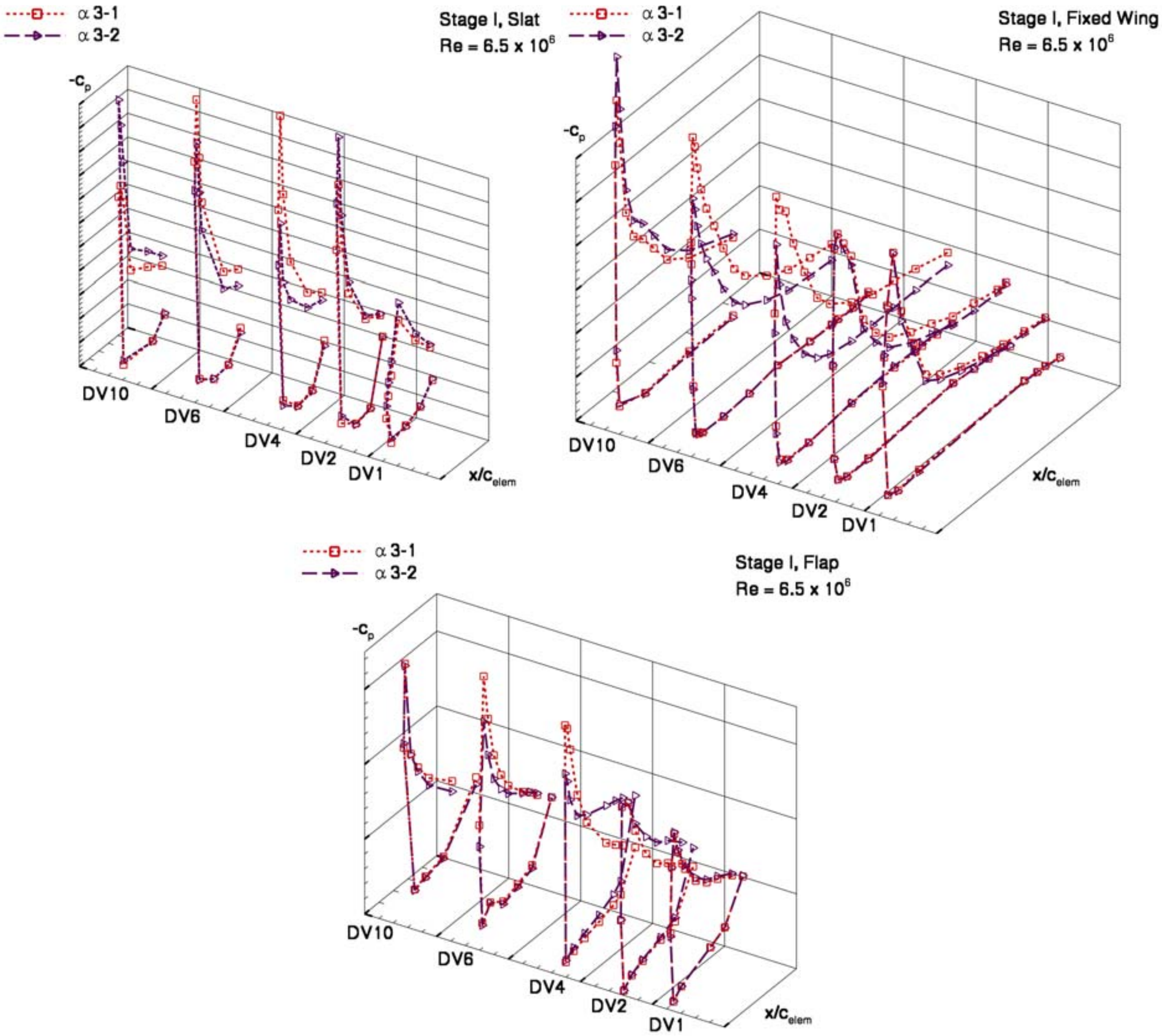

Fig. 14 Pressure distributions slightly and far beyond for low Re-number conditions

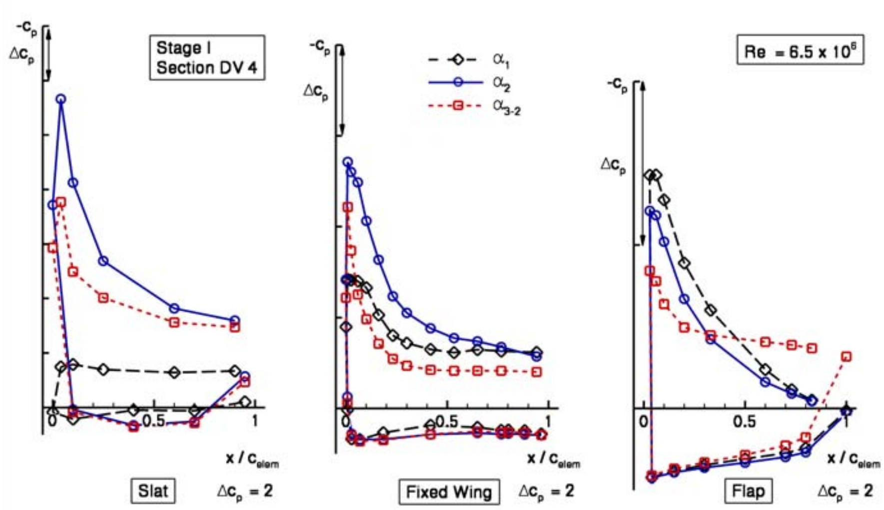

Fig. 15 Midboard pressure distribution at different angles of attack for low Re-number conditions

The lift breakdown between these two angles of attack amounts to 25 lcts. The pressure distributions reveal that this lift loss is dominated by the fixed wing, where clearly a strong trailing edge separation has established for $\alpha_{3\text{-}2}$. Interestingly nearly all suction peaks on the elements have collapsed with the exception of section DV 10, where considerable higher suction peaks are found on the slat and the fixed wing. The reason for this behavior cannot be clarified with the available experimental evidence. The strongest differences are found in section DV 4, so this section is analyzed in more detail in Fig. 15. On the slat a large increase in suction peaks from α_1 to α_2 is found with a $\Delta c_{p(peak)}$ of nearly 10, followed by a considerably smaller value of $\Delta c_{p(peak)} \sim 2.6$ on the fixed wing. On the flap, a decrease in suction peak is found from α_1 to α_2 to $\alpha_{3\text{-}2}$. This behavior is expectedly inline with the observations on the flap for the low Reynolds-number at configuration Stage 0. Following the pressure distribution, trailing edge separation is found on the fixed wing and the flap for $\alpha_{3\text{-}2}$.

The spanwise pressure distributions for the high Reynolds-number case are shown in Fig. 16. The different pressure distributions correspond to a loss in total lift of about 7.5 lcts..

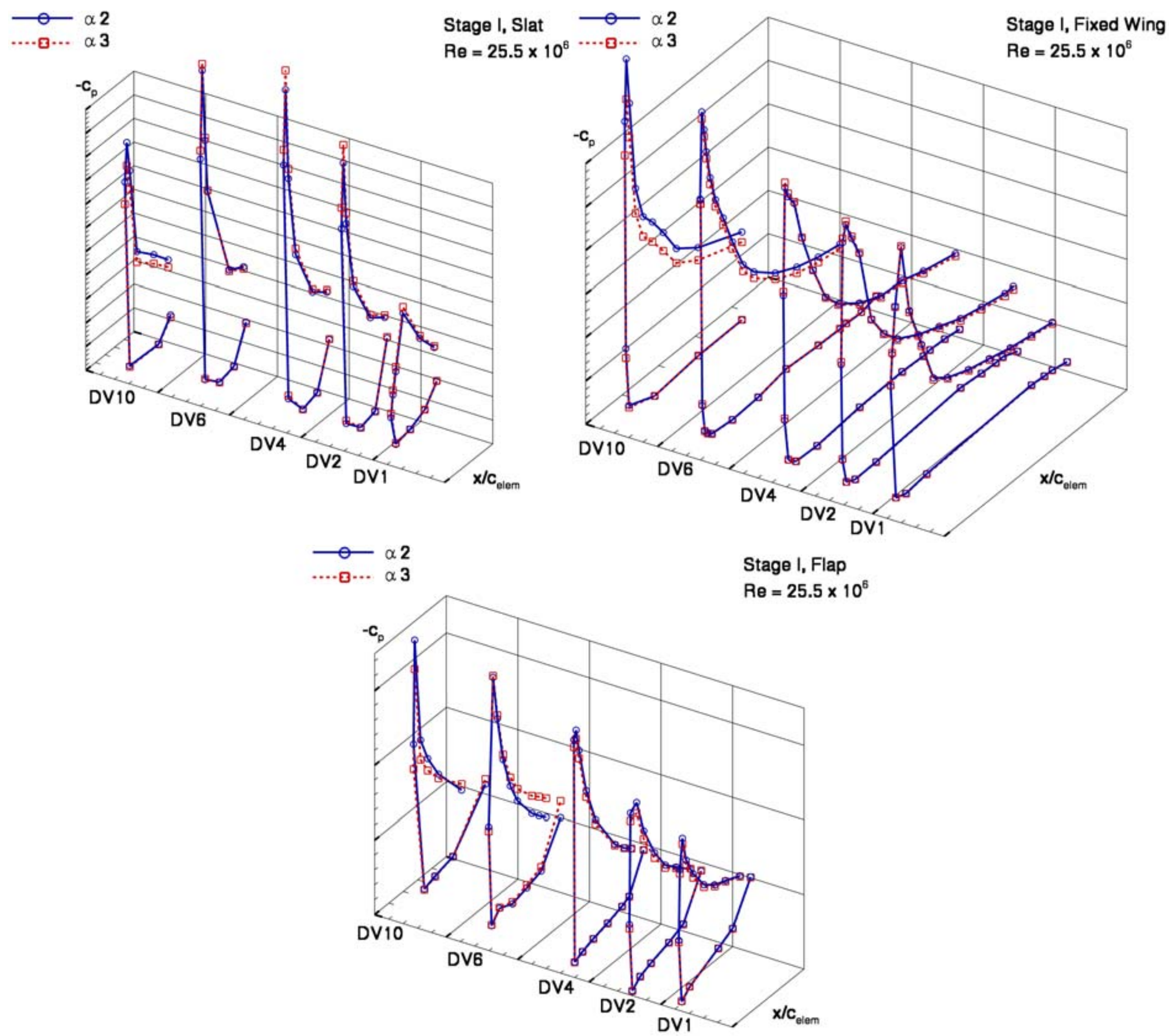

Fig. 16 Pressure distributions at and beyond maximum lift for high Re-number conditions

Taking into account the generally higher magnitude of the suctions peaks due to the higher Reynolds-number, in general the lift breakdown is very similar to the first breakdown of lift as analyzed at the low Reynolds-number condition in Fig. 13. In order to be consistent with the low Reynolds-number case, again section DV 4 is analyzed in more detail in Fig. 17 for the Reynolds-number of Re = 25.5 x 10^6. In accordance with Fig. 16 there is hardly any difference between the pressure distributions for angle of attack of maximum lift α_2 and the one at lift breakdown,

α_3 on all three elements. The increase in suction peaks on the slat between the angle of attack in the linear lift range α_1 and α_2 amounts to $\Delta c_{p(peak)}$ ~ 11.5 and has thus increased by about 15% for the higher Reynolds-number. The other significant difference to the low Reynolds-number case in Fig. 15 is the fact that the trailing edge separation has vanished on the flap for the highest angle of attack. Yet, taking into account the magnitude of lift breakdown in the present high Reynolds-number case it might be more appropriate to compare the change in lift breakdown on the flap to that observed for $\alpha_{3\text{-}1}$ at lower Reynolds-number conditions, see Fig. 13, in which no trailing edge separation is detected either. This underlines that it appears to be crucial to strive for comparable level of lift breakdown if possible, when comparing the pressure distributions at a stall condition after maximum lift has been reached.

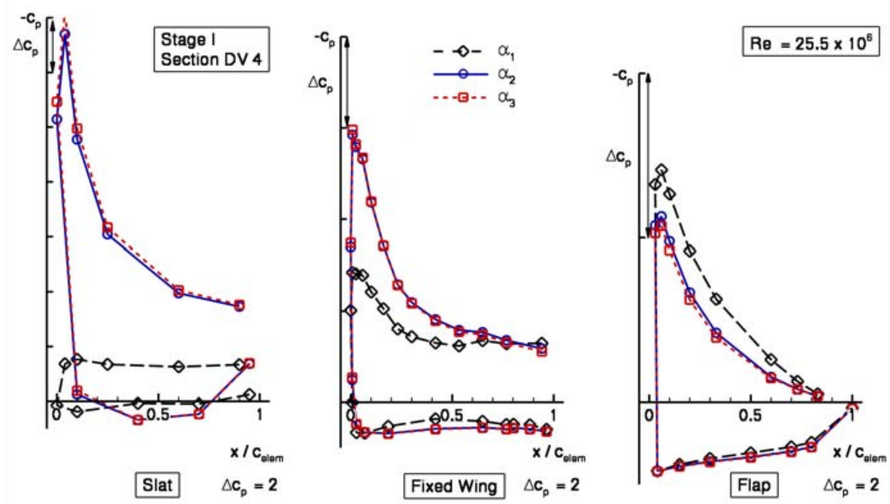

Fig. 17 Midboard pressure distribution at different angles of attack for high Re-number conditions

The analysis of two selected pressure distributions at maximum lift for both Reynolds-numbers is shown in Fig. 18 for the inboard pressure section DV 2, and in Fig. 19 for the respective outboard pressure section DV 10. The main Reynolds-number effect at section DV 10 is an increase in the slat suction peak of $\Delta c_{p(peak)}$ of nearly 2. A similar, although weaker increase in found on the main wing, while on the flap the suction peak is slightly higher for the low Reynolds-number condition. With the exception of the flap, these effects appear to be primary Reynolds-number effects due to the smaller boundary layer displacement thickness on the elements for increased Reynolds-numbers.

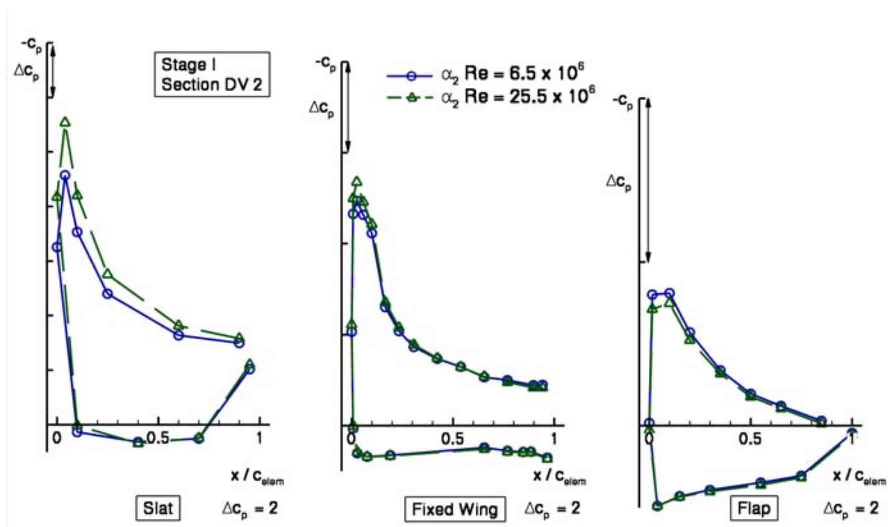

Fig. 18 Inboard pressure distribution at maximum lift for low and high Re-number conditions

In general, the same Reynolds-number trends are found at the outboard section in Fig. 19. The tendency that the slat loading of the outboard wing is decreasing while the loading of the fixed wing and the flap are increasing is not affected by the considerably different Reynolds-numbers.

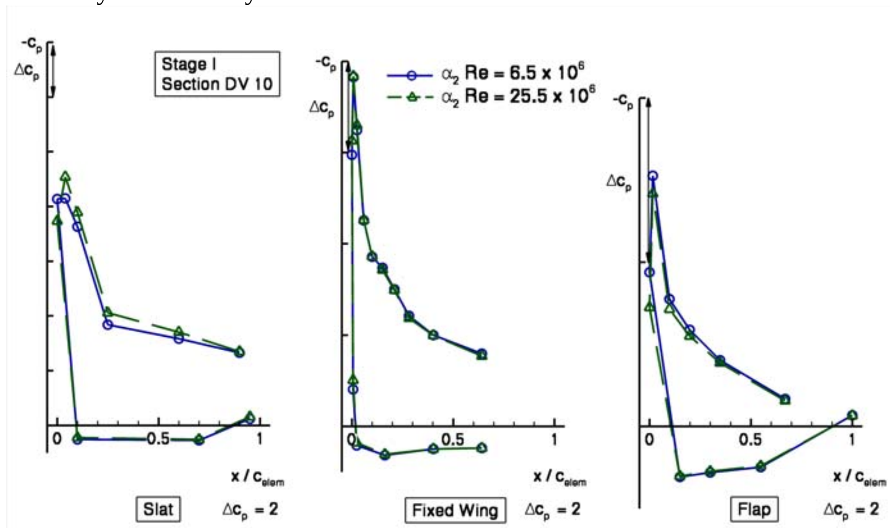

Fig. 19 Outboard pressure distribution at maximum lift for low and high Re-number conditions

C. Configuration KH3Y Complexity Level Stage II

The KH3Y configuration Stage II marks the step from a fuselage with a swept tapered high lift wing to a configuration equipped with nacelle and pylon. The mounting of the pylon necessitates a spanwise cut-out of the slat at the engine position. The limiting Reynolds-numbers and the dynamic pressures as well as the total temperatures are nearly identical to those of configuration Stage I. As noted in Ref. 17 the nacelle and pylon installation usually changes the stall behavior of a high lift configuration, causing the stall to begin somewhere at the fixed wing trailing edge at the spanwise nacelle position. Looking at the corresponding lift curves in Fig. 20 reveals that the most

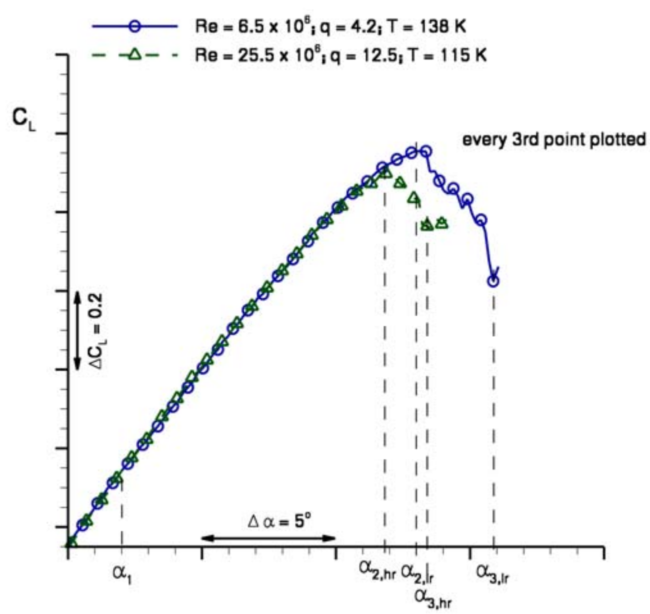

Fig. 20 Lift curve for low and high Reynolds-number for the KH3Y complexity Stage II

striking difference with respect to Reynolds-number effects for configuration Stage II is the appearance of a distinct adverse scale effect. The maximum lift, obtained for the Reynolds-number of Re = 6.5 x 10^6, is nearly 6 lcts. higher than the maximum lift reached at Re = 25.5 x 10^6. Table 4 indicates that the angle of attack at which maximum lift is reached, α_2, is about 1.3^o smaller for the high Reynolds-number, while the angle of attack at clear lift breakdown α_3, is 2.3^o smaller for the high Reynolds-number condition. Following Fig. 20 is has to be noted, that the lift breakdown for the low Reynolds-number condition $\Delta C_L(\alpha_2 - \alpha_3)$ amounts to 0.33, while the evaluated lift breakdown for the high Reynolds-number case is only $\Delta C_L(\alpha_2 - \alpha_3) \sim 0.13$. This is not related to any conceptual aerodynamic effect, but is more related to the availability of data points beyond α_2.

Table 4: Characteristic angles of attack for KH3Y configuration Stage II

Angle of attack		Re = 6.5 x 10^6	Re = 25.5 x 10^6
α_1	[^{o}]	7.04	7.01
α_2	[^{o}]	18.00	16.68
α_3	[^{o}]	20.87	18.57

As shown in Ref. 1 the maximum lift value obtained for Re = 6.5 x 10^6 is also the largest maximum lift value of all evaluated Reynolds-numbers for configuration Stage II. In addition, it can be deduced from Ref. 1 that no clear dependency of maximum lift with Reynolds-number can be derived for this case.

The primary aerodynamic interference of an underwing mounting of a nacelle and pylon on a wing with high lift devices is an interaction of the nacelle vortices with the upper surface of the fixed wing and flap as well as the effect caused by the slat cut-out, see Ref. 17. Typically, as in the present case, the inboard vortex of the nacelle passes over the wing, while the outboard vortex is passing below the wing outboards of the pylon. The upwash induced by the inboard vortex provokes a premature separation on the wing. This is illustrated for the KH3Y configuration Stage II in Fig. 21. by PIV measurements taken through EUROLIFT II low Reynolds-number experiments in the B-LSWT of Airbus-Deutschland[15].

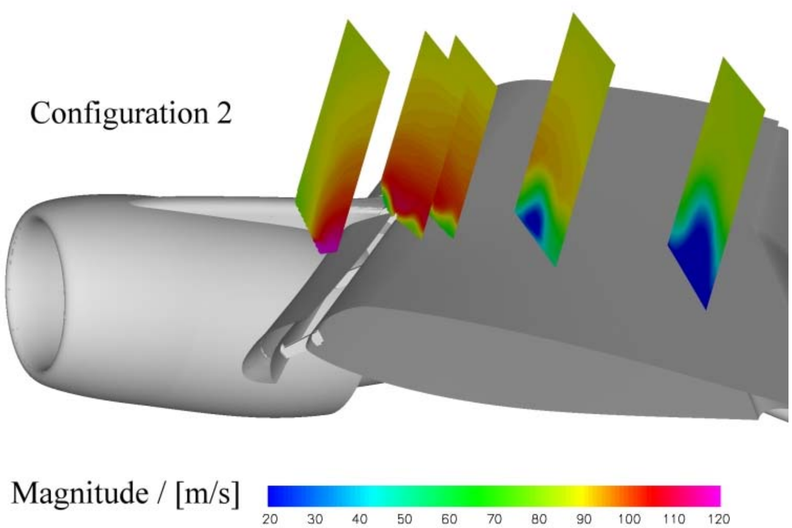

Fig. 21 PIV measurements in the B-LSWT for low Re-number conditions; KH3Y complexity Stage II

The velocity distributions in 5 crossflow planes above the pylon and the fixed wing clearly prove the confined area of low velocity caused by the nacelle vortex. Such type of flowfield evidence is at present not available for the ETW high Reynolds-number measurements. Nevertheless, the basic aerodynamic effects due to the engine/airframe interference are also expected for the flow conditions under investigation.

The pressure distributions along the span are displayed for the low Reynolds-number condition in Fig. 22. The slat is only weakly affected by the stall. The fixed wing exhibits a clear tendency for trailing edge separation, most noticeable at section DV 2, which has the strongest loss in suction peak at α_3. The strong lift breakdown at DV 2 is underlined when comparing the pressure distributions to the corresponding low Reynolds-number measurements of the configuration without nacelle in Fig. 14. As DV 2 is located inboard of the nacelle the observed breakdown of lift is consistent with the interaction of the nacelle vortex and the fixed wing described above. Nevertheless, the loss of lift extends up to the tip of the fixed wing. The flap pressure distributions are less affected, although also here a clear tendency for trailing edge separation is observed at the inboard sections DV 1 and DV 2.

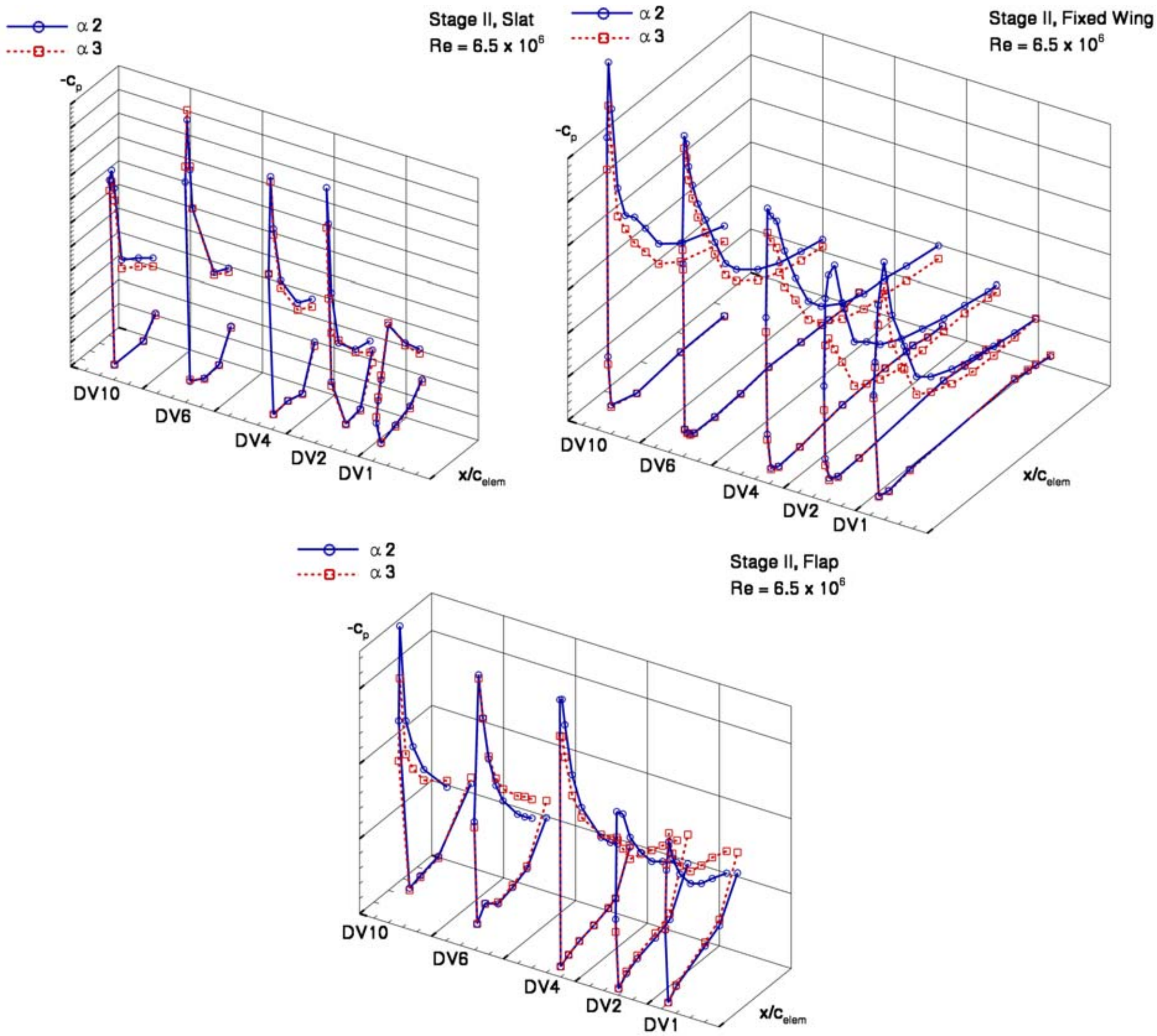

Fig. 22 Pressure distributions at and beyond maximum lift at low Re-number conditions

The development of the pressure distribution at DV 2 for the 3 consecutive angles o attack is depicted in Fig. 23. It becomes more obvious in this graph that also the slat suction peak is collapsing considerably beyond maximum lift. This is tendency has not been found for configuration Stage I, where all slat pressure distribution exhibit at least a constant or increased suction peak for α_{3-1} and especially from α_{3-1} to α_{3-2} , see Fig. 13 and Fig. 14. For the fixed wing and the flap the same general behavior is found as for configuration Stage I, featuring the highest lift generation for α_2 at the fixed wing and at α_1 on the flap.

The corresponding pressure distributions along the span for the high Reynolds-number case are shown in Fig. 24. At first glance no significant differences in the stall behavior of the wing along the span are detected, implying that the general type of lift breakdown is not affected by the increase in Reynolds-number. This leads to the conclusion that the adverse scale effects are not caused by a change in principal stall type.

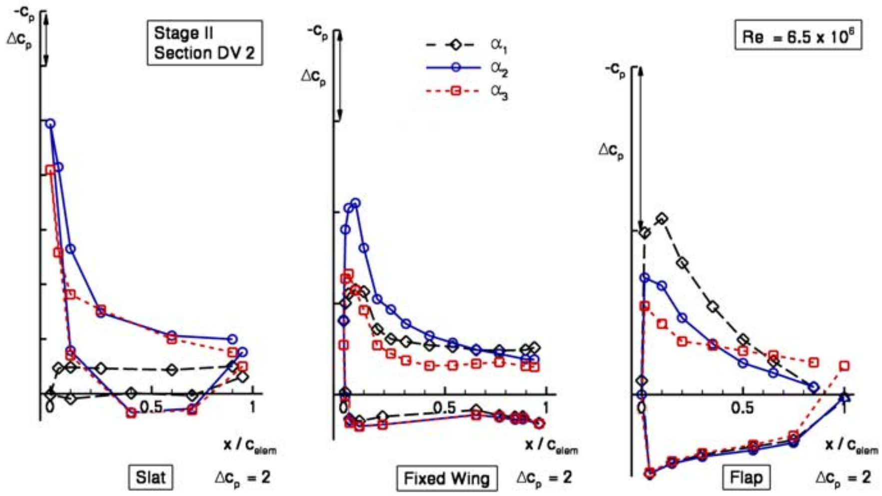

Fig. 23 Inboard pressure distribution at different angles of attack for low Re-number conditions

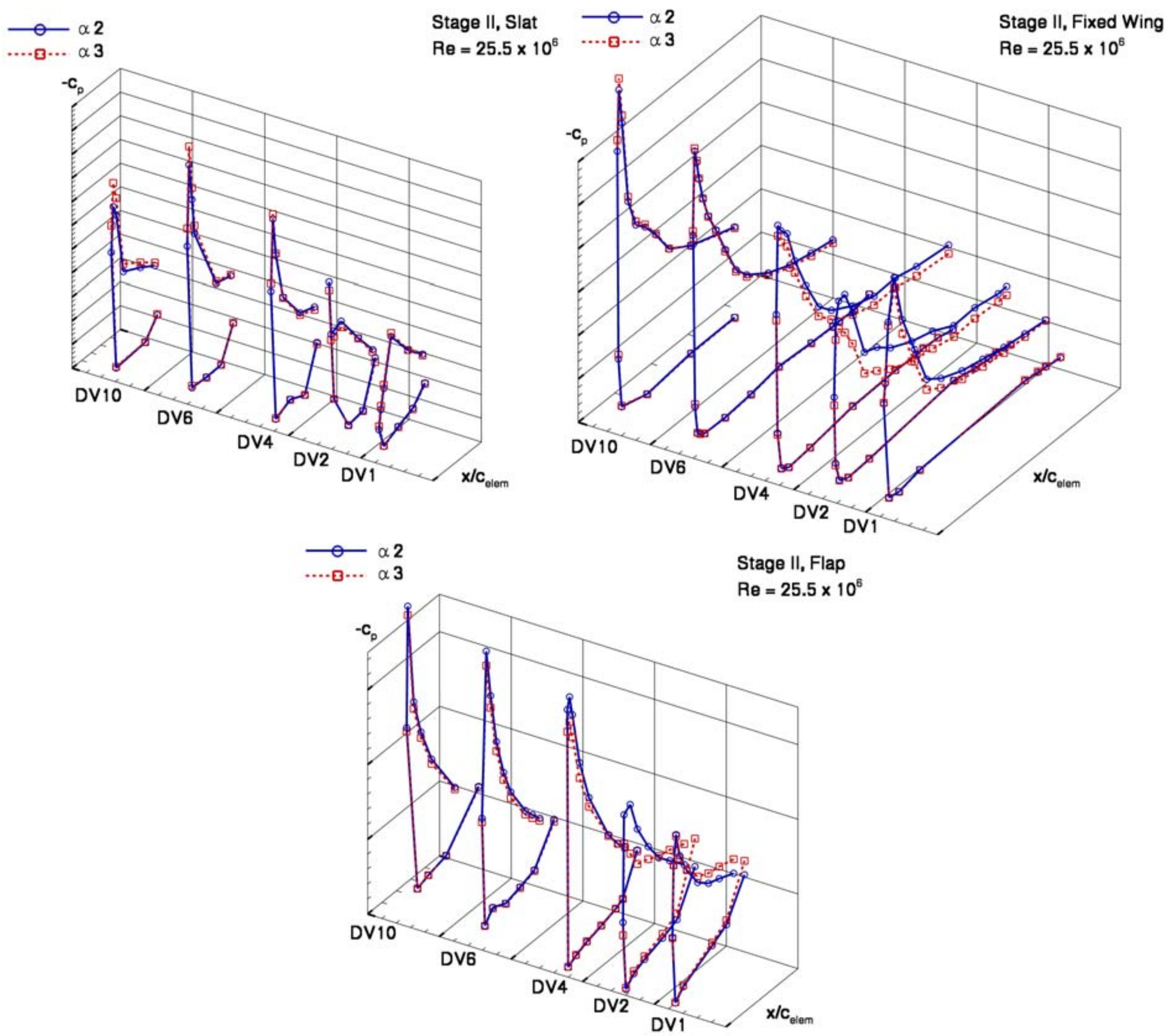

Fig. 24 Pressure distributions at and beyond maximum lift at high Re-number conditions

As for the low Reynolds-number case, the slat is only weakly affected while the most obvious lift breakdown is found on the fixed wing inboard of the nacelle. Also the corresponding flap section DV 2 exhibits a clear trailing edge separation at the incidence beyond maximum lift α_3. Obviously the aerodynamic interaction of the nacelle vortex with the inboard fixed wing upper surface is triggering the stall also for high Reynolds-number. A closer comparison with the results of the low Reynolds-number case at maximum lift reveals that the lift generation on the slat is smaller for the high Reynolds-number conditions. This holds for all evaluated sections except the most inboard one. Interestingly the suction peaks for the slat sections DV 4 and DV 10 are higher for α_3 than for α_2, while there is the opposite trend for the low Reynolds-number results. Again, this is an indication, that not the stall itself is affected by the change in Reynolds-number, but the lift generation on the slat at maximum lift.

This finding is confirmed by the analysis of the critical pressure section for this case, DV 2 in Fig. 25. In accordance with the lift curves the pressure distributions in the linear lift range at α_1 are very similar for both Reynolds-numbers. The comparison to the results of the low Reynolds-number case shows that the slat pressure distribution has considerably changed with a lower suction peak. The slat pressure distribution at α_2 is nearly identical to that at α_3. The sequence and slope of the pressure distributions on the fixed wing and the flap is similar to the low Reynolds-number results.

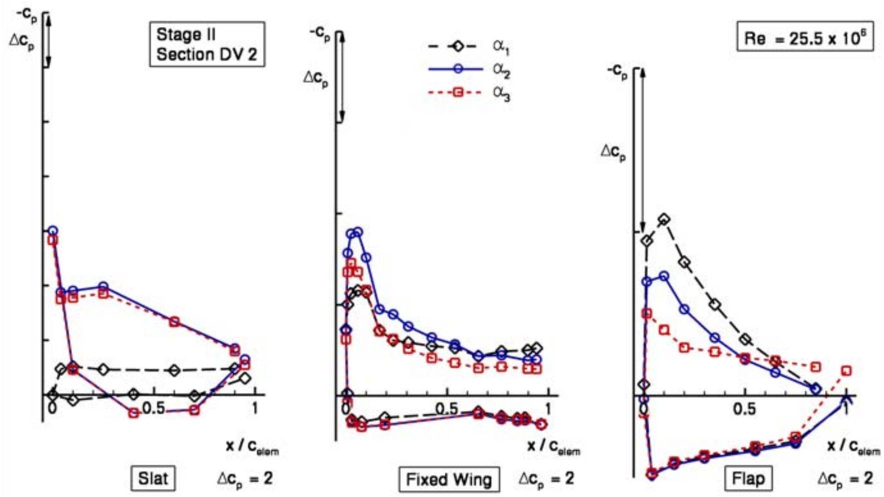

Fig. 25 Inboard pressure distribution at different angles of attack for high Re-number conditions

For the further analysis the cross-plotting of the pressure distributions at maximum lift for both, the low and the high Reynolds-number conditions is especially meaningful, shown at DV 2 in Fig. 26, as well as at DV 4 in Fig. 27.

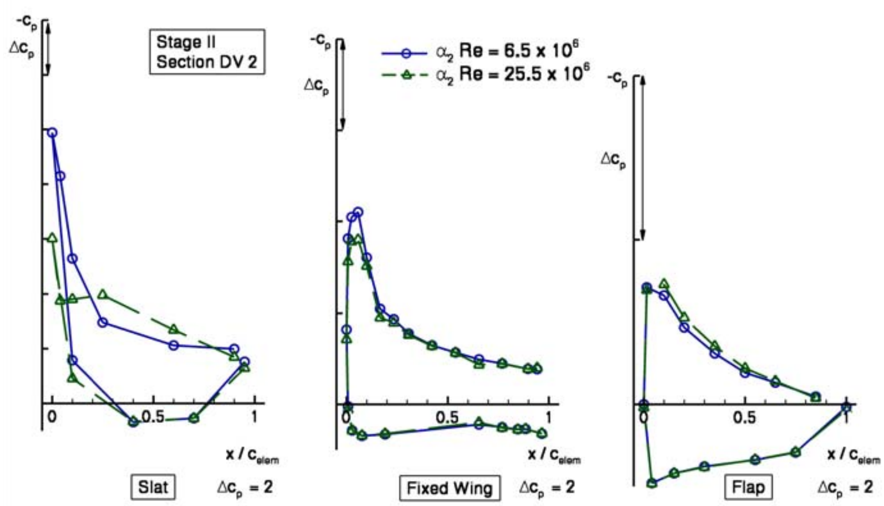

Fig. 26 Inboard pressure distribution at maximum lift for low and high Re-number conditions

In both sections the pressure distributions on the flap are very close to each other. In principle the same holds for the fixed wing, although especially at DV 2 a higher suction peak is observed for the low Reynolds-number condition. The differences in the pressure distributions on the slat are very pronounced, as already indicated throughout the analysis of the spanwise sections. At DV 2 the difference in the suction peaks on the slat between both Reynolds-numbers amounts to $\Delta c_{p(peak)} \sim 4$. A peaky type of pressure distribution is found for both Reynolds-numbers, but most pronounced for the higher Reynolds-number condition. Although the number of pressure tabs on the slat is not large enough for a detailed investigation, the slope of the pressure distribution indicates a leading edge separation bubble.

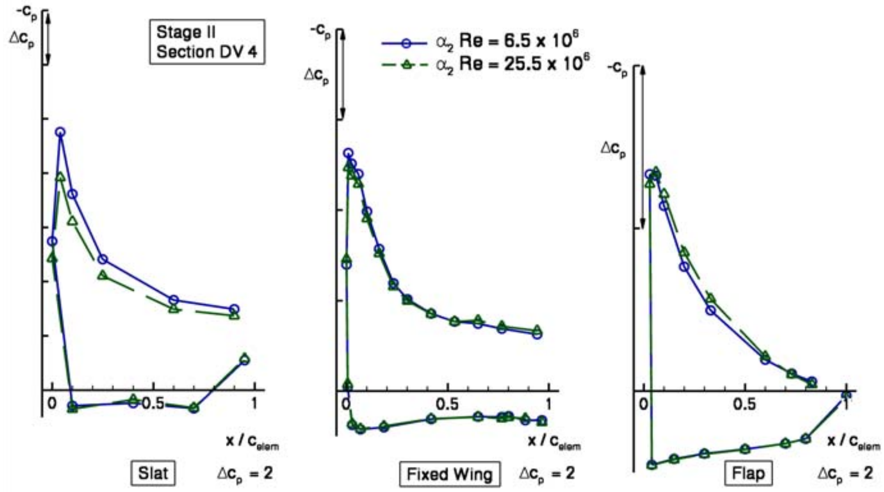

Fig. 27 Midboard pressure distribution at maximum lift for low and high Re-number conditions

This development is not found for the slat pressure distribution at section DV 4 in Fig. 27. The pressure level is lower for the lower Reynolds-number over the complete upper surface. The fact that this type of higher circulation is also found outboards of the nacelle/pylon intersection with the wing demonstrates that the adverse effect caused by the nacelle on the slat is not limited to the vicinity of the nacelle/pylon mounting. As the evaluation of the different spanwise sections shows the complete slat is affected.

D. Configuration KH3Y Complexity Stage III

The final increase in complexity features a strake at the upper inboard portion of the nacelle to the Stage II configuration and is designated as configuration Stage III. The onflow parameters of the limiting Reynolds-numbers are nearly identical to those of the previous two stages. The intended effect of the nacelle strake is to alleviate or eliminate the effect of the nacelle vortices by additional intentionally induced velocities caused by the strake. For this purpose usually the strake position on the nacelle, its size, shape, and inclination have to be optimized. For the present configuration this has been done in a low Reynolds-number wind tunnel test campaign within the framework of EUROLIFT II in the Airbus-B-LSWT, Ref. 15. The resulting lift curves for both Reynolds-numbers for the configuration with strake are shown in Fig. 28. It becomes obvious that the adverse Reynolds-number effect of the two considered limiting Reynolds-numbers for Stage II has turned into a slightly favorable effect, generating an increase in maximum lift of nearly 4 lcts. for the highest Reynolds-number of Stage III. The overcompensation of the adverse Reynolds-number effects observed at Stage II in Fig. 20 has basically two reasons. First, looking at the performance of the strake with Reynolds-number in Fig. 28, the presence of the nacelle strake leads to an increase in α_2 of about 1.3^o for the high Reynolds-number condition, while α_2 for the low Reynolds-number condition remains nearly constant. This is confirmed by the characteristic angles of attack which are listed for both conditions in Table 5. For configuration Stage III α_2 is now nearly identical for both Reynolds-numbers. Moreover, the nacelle strake causes a more linear slope of the lift curve close to α_2 for the high Reynolds-number condition. This results in a less rounded maximum lift range compared to the low Reynolds-number condition. The slope in the post maximum lift regime is fairly similar for both Reynolds-numbers. Second, the assessment of the absolute values of maximum lift with (Stage III) and without (Stage II) reveals, the nacelle strake has a beneficial influence on maximum lift for the present configuration only for the high Reynolds-number case where it improves maximum lift by about 8.5 lcts.. For the low Reynolds-number case the configuration with nacelle strake produces a maximum lift which is smaller

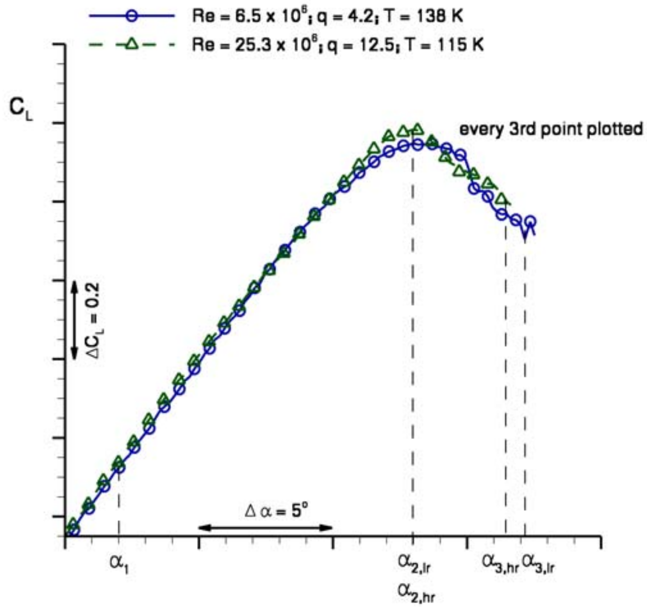

Fig. 28 Lift curve for low and high Re-number for the KH3Y complexity Stage III

by slightly less than 1 lct.. The tendency has already been observed in the discussion of the overall dependency of maximum lift from Reynolds-number in Ref. 1. Like for the Stage II configuration there is no strict dependency of the maximum lift with Reynolds-number for configuration Stage III. The highest absolute maximum lift value of configuration Stage III is generated at Re = 20.3 x 10^6.

Table 5: Characteristic angles of attack for KH3Y configuration Stage III

Angle of attack		Re = 6.5 x 10^6	Re = 25.3 x 10^6
α_1	[°]	7.03	7.00
α_2	[°]	17.99	17.98
α_3	[°]	22.15	21.46

The evaluation of the five selected pressure sections along the span of configuration Stage III is shown for the low Reynolds-number condition in Fig. 29. In contrast to the results of configuration Stage II in Fig. 22, the suction peaks on the slat are higher at α_3 for all considered spanwise sections, indicating that again the slat is not triggering the lift breakdown. The situation on the fixed wing is fairly the same as for the low Reynolds-number case of configuration Stage II with a clear tendency for trailing edge separation in all sections. The influence of the strake after maximum lift gets visible by the fact, that for configuration Stage III the lift breakdown at DV 2 is less pronounced than it has been at DV 2 for configuration Stage II. The flap pressure distributions reveals, that lift break down predominantly is occurring on the inboard and midboard part of the wing (DV 2 – DV 4), again with an indication of trailing edge separation. Also section DV 10 shows a considerable loss of lift. The analysis of the development of the pressure distributions at DV 2 with angle of attack in Fig. 30 confirms this finding. The differences to configurations Stage II are small, most pronounced on the slat. The comparison to the DV 2 pressure distribution for the configuration without strake in Fig. 23 reveals, that with the strake mounted on the nacelle, the suction peak on the slat at maximum lift is smaller by a $\Delta c_{p(peak)}$ ~ 1.7. In parallel, the slat suction peak of configuration Stage III is higher when lift is breaking down at α_3. There is hardly any difference visible for the fixed wing pressure distribution at α_2. This underlines the lack of a beneficial effect of the nacelle strake at maximum lift for the low Reynolds-number condition.

The corresponding pressure distributions along span for the high Reynolds-number conditions are depicted in Fig. 31. Again it is helpful to compare also to the stall behavior of the corresponding configuration without strake at the same Reynolds-number in Fig. 24. The suctions peaks on the slat of configuration Stage III have increased for all

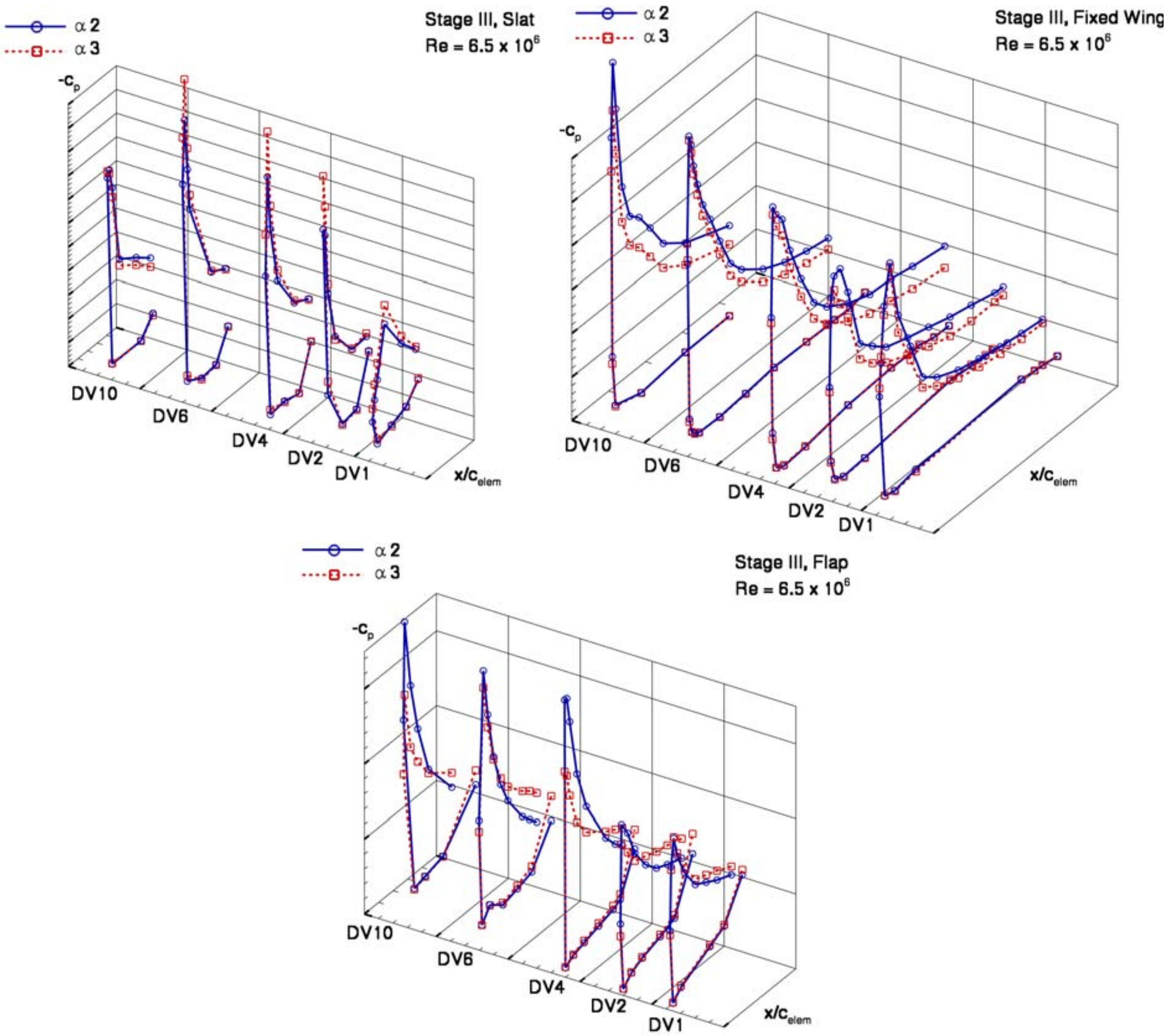

Fig. 29 Pressure distributions at and beyond maximum lift at low Re-number conditions

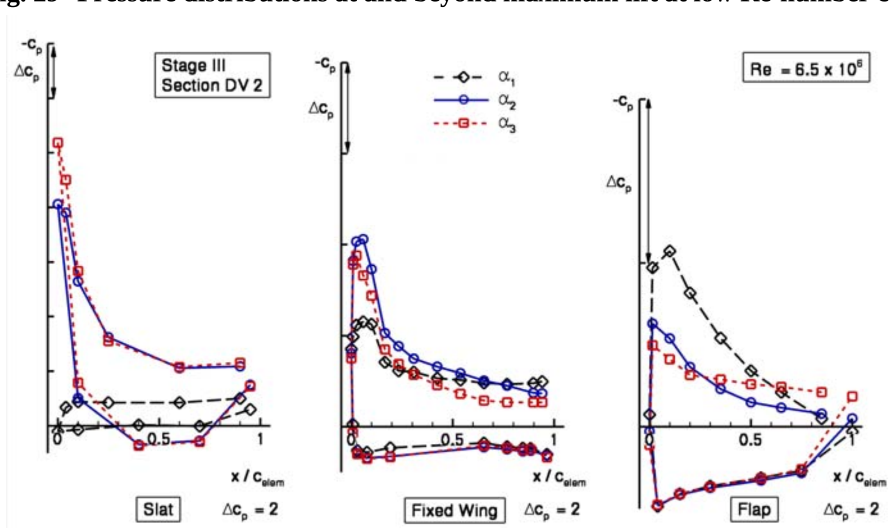

Fig. 30 Inboard pressure distribution at different angles of attack for low Re-number conditions

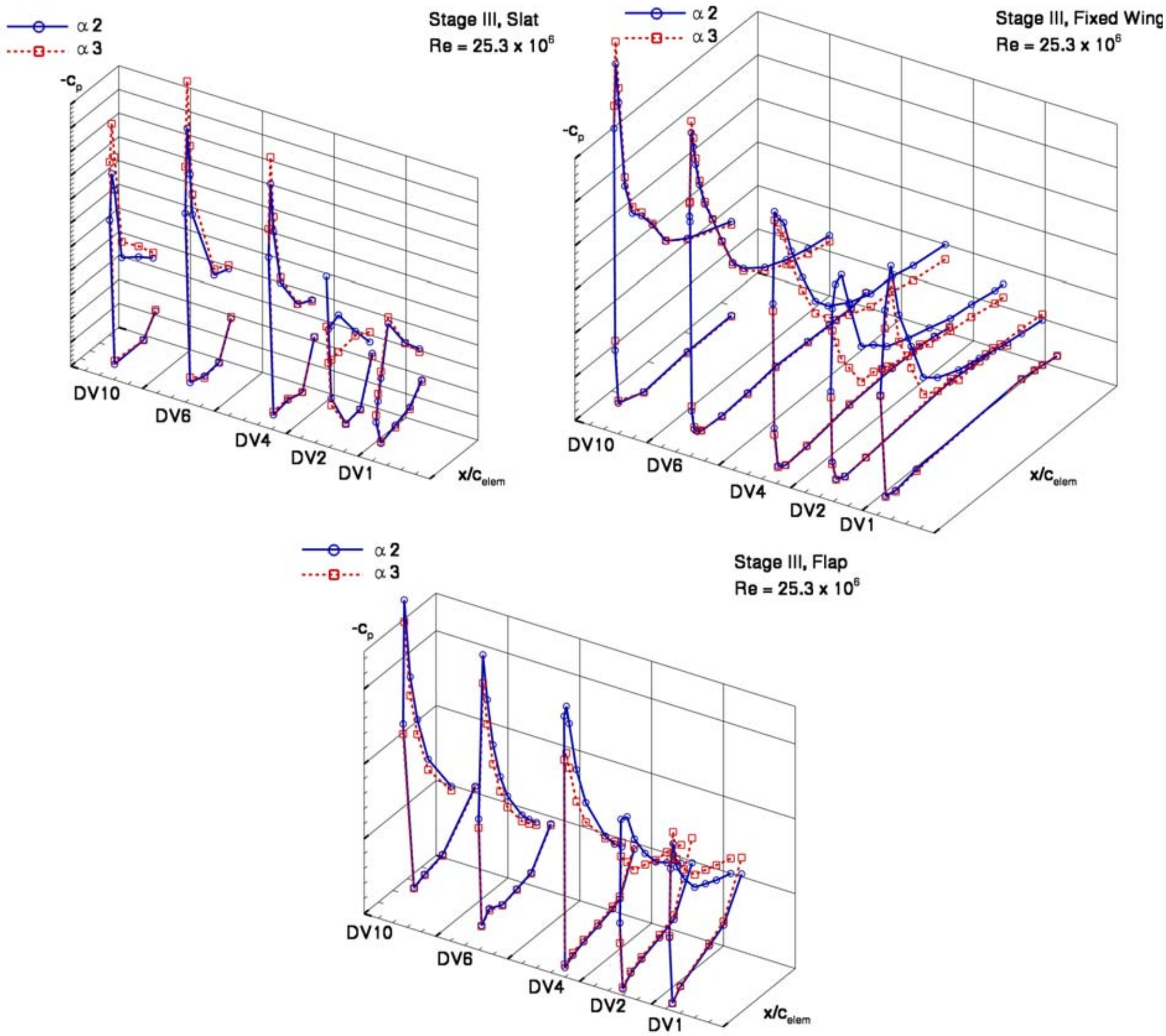

Fig. 31 Pressure distributions at and beyond maximum lift at high Re-number conditions

evaluated sections compared to those of Stage II except for DV 2. This holds for both, the angle of attack at maximum lift, α_2, as well as for the angle of attack at lift breakdown, α_3. The pressure distributions at and beyond maximum lift on the fixed wing reveal that the general trend of the lift breakdown with a trailing edge separation at the sections close to the spanwise nacelle position, DV 2 and DV 4, is generally not changed by the strake. The lift breakdown on the flap is hardly affected by the mounting of the strake. In both cases the two inboard sections on the flap, DV 1 and DV 2, exhibit a distinct trend for trailing edge separation.

Fig. 32 shows the development of the pressure distribution at DV 2 with incidence for the high Reynolds-number case. Consistently this section has to be compared to the one without strake at high Reynolds-number in Fig. 25. In contrast to the low Reynolds-number condition now the slat pressure distribution at maximum lift is not changing due to the presence of the strake. Instead, the lift breakdown beyond maximum lift at α_3 is more severe in Fig. 32. The pressure distribution on the fixed wing exhibits the expected strake effect. Compared with Fig. 25, the suction peak is slightly higher. This can be regarded as the effect of the induced velocities of the strake vortex provoking an alleviation of the typical lift loss in this section due to the nacelle and pylon mounting. It has not been observed for the corresponding low Reynolds-number case. The reason why the strake vortex is not acting in this way at Re = 6.5 x 10^6 cannot be clarified without further insight in the behavior of the strake vortex.

Finally a comparison of the pressure distribution at maximum lift is given for the two limiting Reynolds-numbers at both sections close to the nacelle in Fig. 33 and 34. The pressure distributions for section DV 4 in Fig. 34 lie nearly on top of each other on all three elements. A distinct Reynolds-number influence is only observed at the

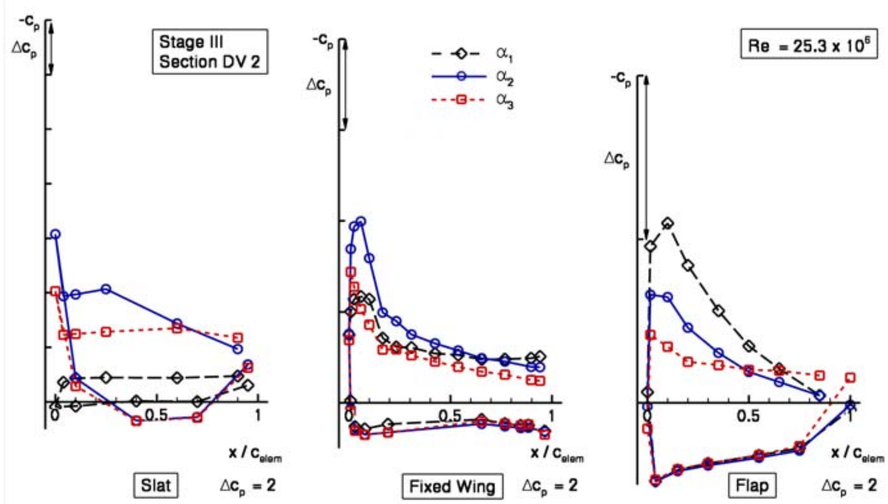

Fig. 32 Inboard pressure distribution at different angles of attack for high Re-number conditions

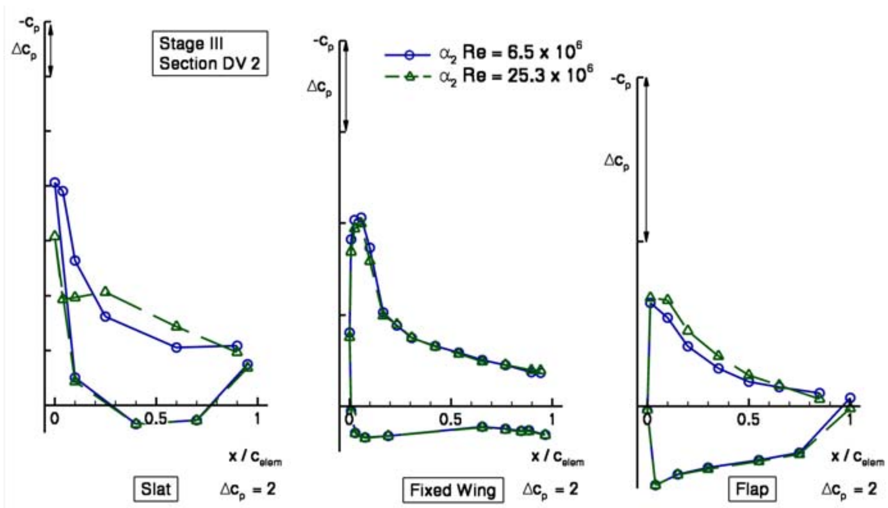

Fig. 33 Inboard pressure distribution at maximum lift for low and high Re-number conditions

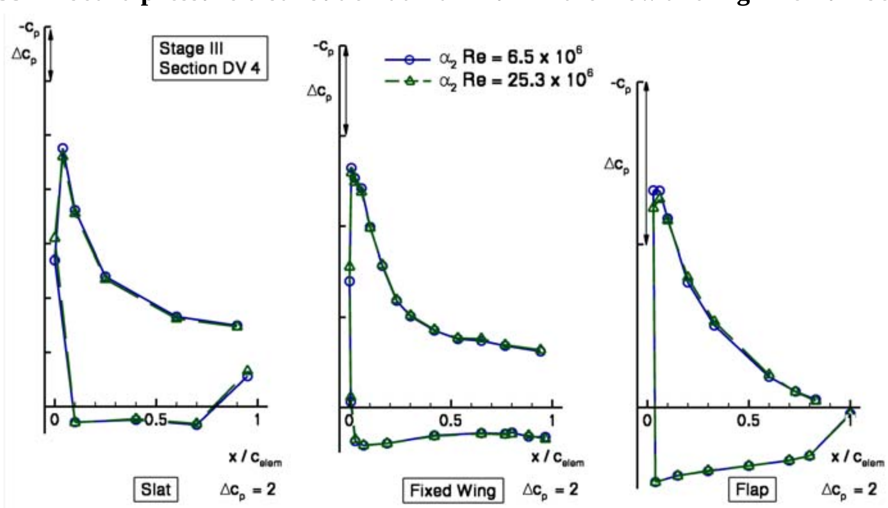

Fig. 34 Midboard pressure distribution at maximum lift for low and high Re-number conditions

inboard pressure section. As seen before, the peaky slat pressure distribution at DV 2 is found independent of the nacelle strake and its vortex at the high Reynolds-number. The pressure distribution of the fixed wing doesn't exhibit a noticeable Reynolds-number effect, while the pressure distribution on the flap shows a lower pressure level on the upper surface for the high Reynolds-number. The reason for the improved maximum lift performance of the configuration with strake at Re = 25.3 x 10^6 becomes obvious, when both pressure sections are compared to the corresponding sections of configuration Stage II in Fig. 26 and Fig. 27. First of all the presence of the strake compromises the slat suction peak for the low Reynolds-number at DV 2. Probably the most important effect is the increase of the fixed wing suction peak at the inboard section for the higher Reynolds-number. Third, compared to the Stage II configuration the suction peak on the slat at the midboard section DV 4 is increased at the high Reynolds-number condition to match the pressure level of the low Reynolds-number case. The scale effects discussed for configurations Stage III are not limited to the two midboard sections. Still it has to be kept in mind that maximum lift for configurations Stages II appears to be extraordinary high at Re = 6.5 x 10^6 with a considerably decrease for Re = 25.5 x 10^6, see Fig. 1 The favorable Reynolds-number influence on the strake effect for the present configuration at the high Reynolds-number condition is comparatively small. It is only a part of the general strake effect.

E. Short Term Repeatability for Configuration KH3Y Complexity Stage II

In order to assess the accuracy and the reliability of the experimental data under investigation, a comparison of two lift curves taken within one test campaign for the same conditions is carried out. As an example configuration Stage II is selected for this purpose. The comparison is done at the lower Reynolds-number of Re = 6.5 x 10^6 for a dynamic pressure of q = 4.2 kPa and a total temperature of T_t = 138 K representing cryogenic conditions. The lift curves shown in Fig. 35 have already been presented in Ref. 11. Harmonized to the focus of the present paper the comparison is now extended by analyzing also pressure distributions at and beyond maximum lift. Especially the area of lift breakdown is of interest, as it is studied on a regular basis in the present investigation. Usually the post maximum lift regime is characterized by considerable portions of separated and thus unsteady flow. So the question of the uncertainty in this flow regime with respect to the reproducibility of the pressure field and the main aerodynamic properties on the wing is essential.

The two lift curves in Fig. 35 reveal a good match in the linear lift regime up to maximum lift. The difference in maximum lift amounts to $\Delta C_{L,max}$ = 0.007 corresponding to 0.25% of the total maximum lift coefficient.

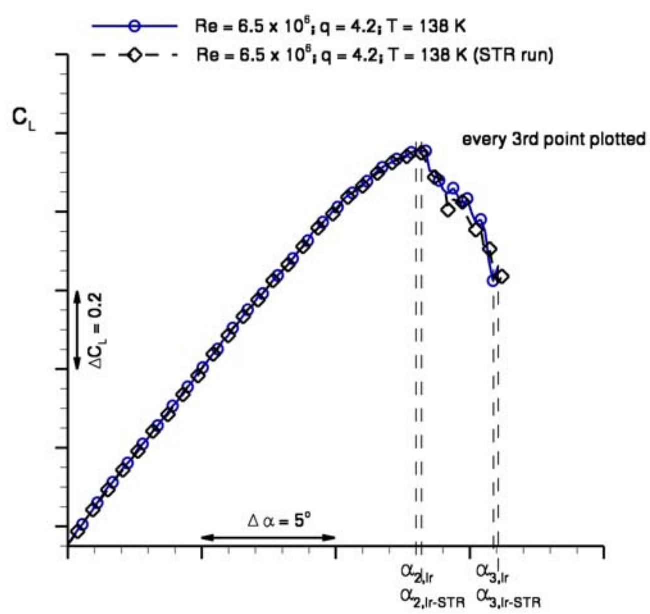

Fig. 35 Lift curves of repeat runs for low Re-number conditions; KH3Y complexity Stage II

As listed in Table 6 the angles of attack for maximum lift, α_2, differ by about 0.2°. The corresponding angles of attack at the chosen lift breakdown angle of attack, $\alpha_{3,}$ differ by about the same amount. The lift curves beyond maximum lift match surprisingly good including some discontinuities in the slope. Therefore it is possible to identify matching points at the lift breakdown condition with a good accuracy.

Table 6: Characteristic angles of attack for KH3Y configuration Stage II

Angle of attack		Re = 6.5 x 10^6	Re = 6.5 x 10^6 (STR)
α_2	[°]	18.00	18.19
α_3	[°]	20.87	21.05

For the evaluation of the pressure distributions of the initial and the repeat run pressure section DV 2 is selected, as it has been identified as the most critical one for the configuration with nacelle and pylon. The pressure distribution for maximum lift is shown in Fig. 36. A very good agreement is found for this condition. The two curves can hardly be distinguished.

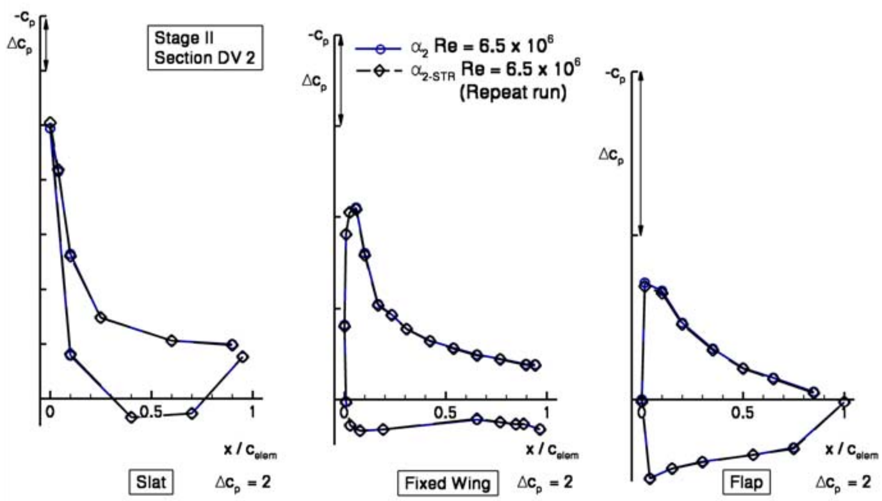

Fig. 36 Inboard pressure distributions at maximum lift for low Re-number conditions

Nearly the same agreement is found for the two pressure distributions at the lift breakdown condition in Fig. 37, although considerable portions of separated flow are expected on this configuration. A slight difference between the two pressure distributions is found on the slat upper surface. As a measure of the repeatability the difference in the pressure coefficient on the slat at the pressure tab located at about 25% local chord amounts to Δc_p = 0.14 corresponding to 4.6% of the measured pressure coefficient.

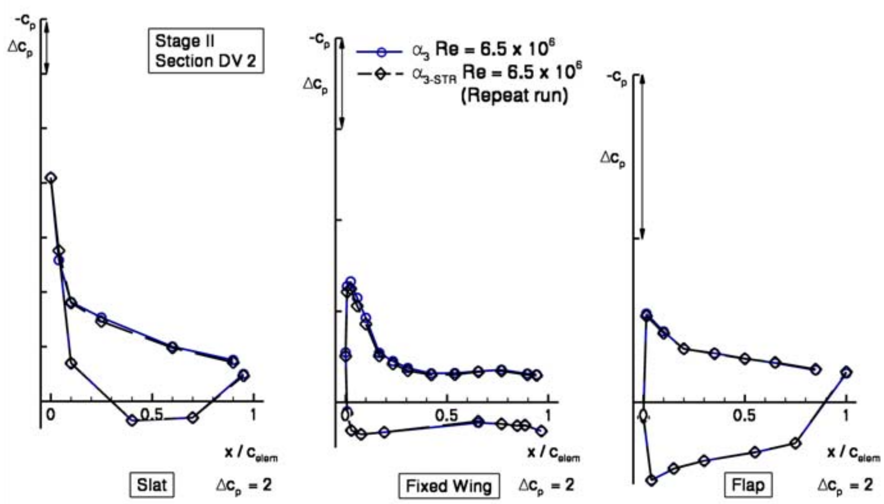

Fig. 37 Inboard pressure distributions beyond maximum lift for low Re-number conditions

IV. Conclusion

Based on a previous analysis of the high lift performance of a wide-body commercial aircraft-type high lift configuration in terms of lift curves and drag polars and their Reynolds-number dependency, a detailed study of the corresponding stall behavior is carried out. The investigation is based on extensive experimental investigations on the aerodynamics of high lift configurations in the European projects EUROLIFT (I) and II. The investigations are conducted using the KH3Y wind tunnel model (DLR F11). The wind tunnel model is designed for a step by step complexity increase up to a complete high lift configuration including pylon, nacelle, and nacelle strake. The wind tunnel data have been gathered in the European Transonic Windtunnel ETW in two different test campaigns. The considered Reynolds-number range extends from Re ~ 2.3 x 10^6 up to cryogenic conditions with Re ~ 25 x 10^6. To analyze the stall behavior spanwise pressure distributions at maximum lift and at lift breakdown together with the corresponding lift curves are compared for two limiting Reynolds-numbers for each configuration.

The angle of attack at lift breakdown is selected arbitrarily. The rationale has been to identify a flow condition with a clear breakdown of lift. The lift breakdown depends on the stall type of the configuration as well as on the availability of experimental data. The difference in lift coefficient between the respective maximum lift values and the lift values at lift breakdown varies for all configurations and flow conditions between ΔC_L = 0.05 and 0.4. In this respect, comparisons between the lift breakdown conditions have to be considered with care. In general extended areas of local flow separation are found beyond maximum lift on the elements of the high lift wing. Given the fact, that for the KH3Y configuration still about 80% or more of the maximum lift value is retained at the breakdown conditions, the overall flowfield can be considered as sufficiently steady to reveal the location and to a certain degree also the mechanism behind the breakdown of lift generation by evaluating time-averaged data.

The most simplified configuration Stage 0 reveals a lift breakdown triggered on the outboard part of the wing. While for low Reynolds-numbers trailing edge separation on the fixed wing and the flap causes the stall, the most significant scale effect is an additional trailing edge separation on the outboard slat. This leads to a more abrupt breakdown in the lift curve. Maximum lift is considerably increasing with Reynolds-number caused by higher circulation on all elements at the outboard sections, eliminating a trend of trailing edge separation on the flap flow at low Reynolds-number conditions.

Introducing the cut-out at the wing/fuselage intersection for configuration Stage I doesn’t change this behavior significantly. No indication is found that the slat-cut-out is triggering the stall on the inboard part of the wing, proving that the slat horn is working efficiently to alleviate adverse effects. Again the stall in terms of type and location is not affected by the Reynolds-number. The most significant local difference is again the vanishing of the trailing edge separation at the outboard section of the flap for the high Reynolds-number condition. The favorable scale effect is mainly produced on the fixed wing and on the flap.

The mounting of nacelle and pylon to configuration Stage I leads to a distinct change in the location of the lift breakdown. It starts for this configuration on the fixed wing inboards of the nacelle and on the inboard part of the flap as a trailing edge separation. This general type and location is not affected by the Reynolds-number. Yet, an interaction of the nacelle vortex with the slat upper surface and the fixed wing leading edge causes a clear adverse Reynolds-number effect.

When adding a nacelle strake for configuration Stage III the lift breakdown inboard of the nacelle is successfully alleviated. Still, the lift breakdown is triggered in the vicinity of the nacelle location on the fixed wing. The interaction of the nacelle strake with the slat in the vicinity of the pylon is working more efficiently at the high Reynolds-number condition. The nacelle strake doesn’t change the principal type of lift breakdown on the KH3Y configuration. Yet, it is quite essential to recall the general Reynolds-number influence on maximum lift in Fig. 1. When comparing configurations Stages II and III the dominating effect is the extraordinary high maximum lift value of configuration Stage II at Re = 6.5 x 10^6 leading to an adverse effect Re = 25.5 x 10^6. The favorable scale effect of the strake for the two Reynolds-numbers is comparatively small.

For none of the four configurations a significant change of the stall type is observed for the considered low and high Reynolds-number conditions. The effects are typically seen in a suppression of flow separation on elements of the high lift system. Short repeatability of the lift curves is good. The comparison of the pressure distributions at maximum lift and especially beyond maximum lift underlines the reliability of the experimental data.

Acknowledgments

The author likes to thank Jürgen Quest, ETW, and Eric Germain, formerly ETW, for providing the experimental data and their active role throughout the ETW tests. The research work discussed in the paper was performed under the European research contract G4RD-CT-1999-00072 in the project EUROLIFT as part of the 5th framework programme, and under contract AST2–2004–502896 in the project EUROLIFT II as part of the 6th framework programme. The author appreciates the European Commission for co-funding this research activity as well as all involved EUROLIFT partner.

References

[1] Rudnik, R., Germain, E., "Re-No. Scaling Effects on the EUROLIFT High Lift Configurations", *AIAA Meeting Paper,* AIAA 2007-0752, 2007.

[2] Eliasson, P., Catalano, P., et. al., "Improved CFD Predictions for High Lift Flows in the European Project EUROLIFT II", *AIAA-2007-4303*, 2007

[3] Quix, H., Schulz, M. et. al., "Low Speed High Lift Validation Tests Within the EC Project EUROLIFT II", *AIAA-2007-4298*, 2007

[4] Moens, F., Perraud, J., et. al., "Transition Prediction and Impact on 3D High-Lift Wing Configuration", *AIAA-2007-4302*, 2007

[5] Wild, J., Brezillon, J., et. al., "Advanced High-Lift Design by Numerical Methods and Wind Tunnel Verification within the European Project EUROLIFT II", *AIAA-2007-4300*, 2007

[6] Hansen, H., Thiede, P., Moens, F., Rudnik, R., and Quest, J., "Overview About the European High Lift Research Programme EUROLIFT", *AIAA Meeting Paper,* 2004-0767, 2004.

[7] Rudnik, R., Thiede, P., "European Research on High Lift Aircraft Configurations in the EUROLIFT Projects", *CEAS/KATnet Conference on Key Aerodynamic Technologies*, CP, 2005, pp. 16.1-16.8.

[8] Rudnik, R., Frhr. v. Geyr, H., *The European High Lift Project EUROLIFT II – Objectives, Approach, and Structure*, AIAA 2007-4296, 2007

[9] MacIntosh W., Wimpress, J. E., "Prediction and Analysis of the Low Speed Stall Characteristics of the Boeing 747", *AGARD-LS-74,* 1975.

[10] Flaig A, Hilbig R., "High-lift design for large civil aircraft", *AGARD High-Lift System Aerodynamics*, CP 515, Sept. 1993, pp. 31-1–31-12.

[11] Van Dam, C. P., "The aerodynamic design of multi-element high-lift systems for transport airplanes", *Progress in Aerospace Scienes*, 38, 2002, pp. *101–144*.

[12] Thibert, J. J., "The GARTEUR High Lift Research Programme", *AGARD-CP-515 High Lift System Aerodynamics*, 1993, pp. 16-1 – 16-21

[13] Johnson, P. L., Jones, K. M., Madson, M. D., "Experimental Investigation of a Simplified 3D High Lift Configuration in Support of CFD Validation", *AIAA Meeting Paper,* AIAA 2000-4217, 2000.

[14] Murayama, M., Imamura, T., Yamamoto, K., "Comparison of Reynolds-Averaged Navier–Stokes Simulations of Multi-Element High-Lift Configurations", *Journal of Aircraft,* Vol. 44 No. 1, 2007.

[15] Neitzke, K.-P., Rudnik, R., Schröder, A., "Low Speed Validation Tests on Engine/Airframe Integration Within the EC Project EUROLIFT II", *AIAA Meeting Paper,* AIAA 2005-3704, 2005.

[16] Gault, D. E., "A Correlation of Low Speed, Airfoil Section Stalling Characteristics with Reynolds-Number and Airfoil Geometry", *NACA TN 3963*, 1957.

[17] Haines, A. B., "Scale Effects at High Lift and Low Speeds", *AGARD-AG-323 Scale Effects on Aircraft and Weapon Aerodynamics* edited by Young, A. D., 1999, pp. 27 – 65